https://doi.org/10.5194/egusphere-2026-815
Preprint. Discussion started: 23 February 2026

The Dual Effect of Urban Areas on Supercell Storms

Francesco De Martin[a,b,c], Christopher Rozoff[c], Andrea Zonato[d], Stefano Alessandrini[c], and Silvana Di Sabatino[a]

[a]Department of Physics and Astronomy, Alma Mater Studiorum, University of Bologna, Bologna, Italy
[b]School of Meteorology, University of Oklahoma, Norman, Oklahoma
[c]U.S. National Science Foundation, National Center of Atmospheric Research, Boulder, Colorado
[d]CIMA Foundation, Savona, Italy

Correspondence: Francesco De Martin (fdemartin@ou.edu, francesco.demartin2@unibo.it)

Abstract. The effect of urban land use on convective storms with deep and persistent rotating updrafts (supercell storms) is systematically investigated using ensembles of idealized numerical simulations. A supercell is simulated over a flat domain containing a circular city surrounded by croplands. It is triggered upstream of the city so that it subsequently moves into the urban area. Twenty-five experiments with eleven ensemble members each are conducted in which city size, urban fraction, building height, and building density are varied. The results show a statistically significant weakening of the supercell with increasing city size. A similar trend is observed when varying building density and urban fraction, although these effects are not statistically significant lower than zero. The weakening of the approaching storm is primarily driven by the urban dry island (UDI), which substantially reduces convective available potential energy. While the initial storm can be suppressed by the city, the urban heat island (UHI) generates a pressure minimum that can trigger a new supercell downwind of the city. Compared with UHI-induced vertical velocities, the building-generated vertical velocities are negligible. This study provides a benchmark that expands our understanding of the complex interactions between the urban environment and deep moist convection, emphasizing the role of the UHI and UDI in influencing storm dynamics and highlighting the potential dual effects of urban land use on supercell storms.

1 Introduction

The most severe socio-economic impacts of severe storms typically occur when they strike urban areas, where large populations are at risk of injuries, and dense infrastructure and numerous vehicles are exposed to damage (e.g., Heimann and Kurz 1985; Wurman et al. 2007). This underscores the need for a thorough examination of the interactions between urban land use and severe storm behavior, with the ultimate goals of improving early warning systems, designing effective emergency plans, informing the public about associated risks, and strengthening socio-economic resilience.

It is well established that the presence of buildings and urban materials significantly modifies the Planetary Boundary Layer (PBL), leading to the Urban Heat Island (UHI; i.e., higher temperatures within cities, Oke 1982), the Urban Dry Island (UDI; i.e., lower relative humidity within cities, Hao et al. 2023), and shifts in streamlines (Britter and Hanna, 2003), which often result in weaker surface winds over urban areas. Furthermore, the existence of an Urban Rainfall Effect (URE) was already noted more than 50 years ago (Changnon and Ackerman, 1977). This phenomenon is associated with altered precipitation patterns driven by urban land use and is typically characterized by enhanced precipitation downstream of both large and compact urban areas (Liu and Niyogi, 2019; Yang et al., 2024).

Several hypotheses have been proposed to explain the URE phenomenon, ranging from thermodynamic mechanisms (UHI-induced vertical motions that trigger convection; Thielen and Gadian 1997; Rozoff et al. 2003), to dynamic processes (vertical velocities induced by flow modifications caused by buildings; Yang et al. 2021a; Bornstein and LeRoy 1990), and chemical reasons (urban aerosols affecting rainfall efficiency; Lin et al. 2011; Fan et al. 2020). In particular, the dynamic explanation has received considerable attention. Various mechanisms have been proposed to explain enhanced vertical velocities resulting from building-induced flow modifications, including dynamical blocking of the flow upstream of buildings (Dou et al., 2024; Shen and Yang, 2023; Yang et al., 2021a; Zhang et al., 2017), flow merging downstream of cities (Shen and Yang, 2023; Dou et al., 2015), downstream wind convergence driven by a pressure minimum induced by flow bifurcation (Yang et al., 2021b), and storm splitting via the so-called building-barrier effect (Dou et al., 2015; Bornstein and Lin, 2000). However, these hypotheses have generally not been tested quantitatively. While it is reasonable to expect that all these factors may influence a convective cell to some extent, it remains unclear whether one (or some) of them plays a dominant role in producing the URE phenomenon.

Moreover, most of these studies have focused on ordinary convective cells, while only a limited number have examined the effects of urban land use on local severe storms. In particular, the present study focuses on supercells, which are convective storms with a deep and persistent rotating updraft and represent the most dangerous type of local severe storm (Homeyer et al., 2025). Since supercells are fueled primarily by air masses located in the lowest few hundred meters of the troposphere (Coffer et al., 2023), it is reasonable to hypothesize that they may be influenced as well by urban land use (Shepherd, 2013). Indeed, some case studies have found that supercells occurring over the US Great Plains were intensified by the presence of cities (Reames and Stensrud, 2018; Lin et al., 2021; Fan et al., 2023). Similarly, Platonov et al. (2024) reported a systematic increase in updraft helicity (UH) over Moscow (Russia) compared to simulations without the city. A recent work showed that even a Quasi-Linear Convective System (QLCS) can be displaced and broken by the urban land use (De Martin et al. 2025).

Attempts to generalize these pioneering case studies have been made using idealized simulations (Naylor, 2020; Naylor and Mulholland, 2023; Naylor et al., 2024), which found that both supercells and QLCSs intensified when a city was included. However, in those simulations, the city was simplified as a thermal and roughness perturbation, and a realistic city was not considered in the simulation domain.

These early investigations suggest that even local severe storms can be modified by urban land use. Nevertheless, they either lack generality or rely on overly simplified urban representations. Therefore, the present research employs idealized simulations using state-of-the-art urban parameterizations to better assess whether urban perturbations are sufficiently strong to alter supercell behavior. Another important aspect that has been only marginally addressed in previous studies concerns the physical processes responsible for urban-induced modification of supercells. Accordingly, this research is guided by two main scientific questions:

1. Can a city modify a supercell?

2. What are the physical processes that cause such modifications?

The limitation of idealized simulations is that they rely on the outcomes of a numerical model, which must be trusted. To enhance the trustworthiness of the idealized simulations, the similar model settings used for a real case study by De Martin et al. (2025) are employed in the present study.

The analysis is divided into two main phases. The primary objective of the first phase is to investigate how an already developed supercell is modified by the presence of a city. To this end, the storm is initiated upstream and advected toward the city center, where an urban boundary layer has developed during the preceding hours. In particular, we aim to assess the storm's sensitivity to variations in city size, urban fraction, building height, and building density. The second phase of the analysis focuses on understanding how the pre-storm environment is influenced by different urban morphological configurations. This aspect is crucial for explaining the urban-induced storm modifications identified in the first phase.

The methodology used is described in detail in Section 2. The results of the first phase are presented in Section 3, while those of the second phase are shown in Section 4. Finally, the main outcomes of both phases are discussed in Section 5, along with comparisons with the existing literature. Tentative answers to the scientific questions posed above will be provided in Section 6.

2 Method

2.1 Numerical simulation setup

Numerical simulations are performed using version 4.6.1 of the Weather Research and Forecasting (WRF) numerical model (Skamarock et al., 2019). Numerical simulations are conducted in a single square domain with horizontal grid spacing of 1 km, consisting of 250×250 grid points. The same 64 vertical levels used in De Martin et al. 2025 are employed, as they were shown to accurately reproduce severe storm dynamics in a real urban setting. Periodic Boundary Conditions (PBCs) are implemented. A sufficiently large domain is chosen to ensure that spurious wave interactions do not occur during the period analyzed in this study.

The simulations are initialized at 10:00 am (local time), and the storm is triggered at 04:00 pm, a typical initiation time of convection (Manzato et al., 2022). The supercell is initiated using a thermal bubble released at 04:00 pm near the bottom-left corner of the domain, at grid point (40, 40). The bubble is a thermal perturbation of +3 K released at 1800 m AGL. The perturbation relaxes to zero with a vertical radius of 1800 m and a horizontal radius of 10 km. This setup allows the storm to develop for approximately two hours before reaching the city. This numerical configuration is similar to that used by Markowski and Dotzek (2011) to investigate interactions between supercells and idealized orography.

The microphysics scheme used is Morrison et al. (2009), with hail as the prognostic rimed ice species. Longwave radiation is parameterized using the Rapid Radiative Transfer Model (Mlawer et al., 1997), while shortwave radiation is parameterized using the Dudhia scheme (Dudhia, 1989). Radiative forcing corresponds to conditions at a latitude of 45°N (the same as Milan) on May 31st. Noah-MP is used as the land surface model (Niu et al., 2011; Yang et al., 2011), while the Revised MM5 scheme (Jiménez et al., 2012) is employed to resolve the surface layer processes.

Several schemes are tested for the representation of PBL processes, coupled with the 1.5 TKE closure ($km\_opt = 2$ in the WRF namelist), including the Boulac (Bougeault and Lacarrere, 1989), Yonsei University (YSU, Hong et al. 2006), or Mellor-Jamada-Janjic (Janjić, 1994) schemes. Since no remarkable differences are observed among the PBL schemes considered, the YSU scheme is preferred because it is widely used in severe storm studies at mid latitudes and also in urban settings (e.g., Reames and Stensrud 2018).

The domain is entirely flat, with croplands as the uniform land-use category, except for a circular city centered at grid point (90,76). This location is chosen based on an analysis of the supercell evolution in the *no_urban* control run, where the land use is cropland everywhere. The goal is to locate the city such that the supercell passes over its center two hours after initiation, coinciding with the time of peak intensity. Urban surface processes are resolved using the Building Effect Parametrization (BEP, Martilli et al. 2002) and the Building Energy Model (BEM, Salamanca et al. 2010), the most accurate parameterizations of urban processes in mesoscale modeling. In this work, the *sea_breeze_2d*, adapted to run with the BEP-BEM scheme in a three-dimensional domain (Zonato et al., 2021; Pappaccogli et al., 2020), was employed.

2.2 Choice of the input sounding

The choice of the input sounding is carefully addressed. A spin-up time is needed in the simulations to permit the generation of the urban boundary layer. During this spin-up time, deep moist convection is not desired. To achieve the desired controlled experiment, the Weisman-Klemp supercell sounding profile (Weisman and Klemp, 1982) is used. Since the radiative heating during the day quickly triggers deep moist convection, an artificial thermal inversion of 4 K is added in the profile to coincide in height with the lifting condensation level (LCL, Fig. 1a). Through trial and error, an increase of 4 K is chosen as the threshold that completely suppresses the development of moist convection. The same issue was addressed similarly by Nowotarski et al. (2014) and Boyer et al. (2025). At the LCL, the relative humidity is also reduced by a factor of 1.5, to resemble the presence of an Elevated Mixing Layer (EML, see Fig. 1 of Emanuel 2023), a frequent feature during severe storm events both in the US (Andrews et al., 2024) and in Europe (Dahl and Fischer, 2016). The denominator 1.5 is chosen in order to decrease the mid-level moisture, without drying the troposphere excessively. A thermal inversion of 4 K is compatible with real EML profiles (Tuckman and Emanuel, 2024)[1]. Thus, the vertical profile of potential temperature $\Theta(z)$ of the input sounding is defined as:

$$\Theta(z) = \begin{cases} \Theta_0 + (\Theta_{tr} - \Theta_0)\left(\frac{z}{z_{tr}}\right)^{\frac{5}{4}} & z < z_{lcl} \\ \Theta_0 + (\Theta_{tr} - \Theta_0)\left(\frac{z}{z_{tr}}\right)^{\frac{5}{4}} + 4K & z_{lcl} \le z \le z_{tr} \\ \Theta_{tr} exp\left[\frac{g}{C_p T_{tr}}(z - z_{tr})\right] + 4K & z \ge z_{tr} \end{cases} \tag{1}$$

---

[1] Note that the thermal inversion and moisture decrease associated with an EML are usually located at an elevation higher than the LCL. We place them at the LCL because the daytime growth of the PBL lifts the hygrothermal discontinuity to a more realistic elevation.

https://doi.org/10.5194/egusphere-2026-815
Preprint. Discussion started: 23 February 2026

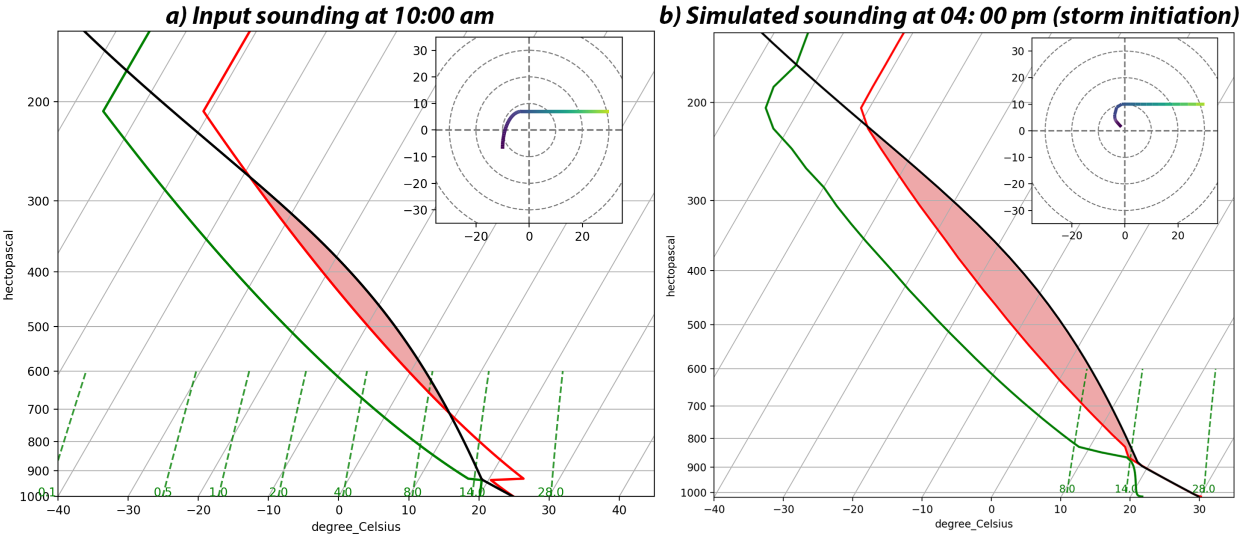

Figure 1. (a) Input sounding at 10:00 am; (b) simulated sounding at 04:00 pm when the storm is initiated with a thermal bubble. Temperature (red line), dew point temperature (green line), and temperature of a surface parcel lifted adiabatically (black line) are shown. The CAPE area is red shaded. The hodograph is shown in the upper-right panel (the first 6 km of wind speeds are plotted).

where g is gravity acceleration, C_p the specific heat capacity of the atmosphere, $\Theta_0 = 296$ K the potential temperature at the surface, $z_{tr} = 12000$ m the height of the tropopause, z_{lcl} is the height of the LCL, $\Theta_{tr} = 343$ K the potential temperature at the tropopause and $T_{tr} = 219$ K its temperature.

The vertical profile of relative humidity $rh(z)$ is defined as:

$$rh(z) = \begin{cases} 1 - \frac{3}{4}\left(\frac{z}{z_{tr}}\right)^{\frac{3}{4}} & z \leq z_{lcl} \\ \left[1 - \frac{3}{4}\left(\frac{z}{z_{tr}}\right)^{\frac{3}{4}}\right]/1.5 & z_{lcl} \leq z \leq z_{tr} \\ 0.25/1.5 & z \geq z_{tr} \end{cases} \tag{2}$$

An exponent of 0.75 is used instead of the 1.25 employed in the original version of Weisman and Klemp (1982), in agreement with Markowski and Dotzek (2011). The moisture in the boundary layer is defined by fixing a maximum value for specific humidity $q_{bl} = 14.5$ g kg^{-1}.

Six hours after the start of the simulation, the solar heating deepens the PBL (Fig. 1b), eroding the thermal inversion and creating high Convective Available Potential Energy (CAPE) values, as expected by the conceptual model of Emanuel (2023). At this time, the convective inhibition is negligible, and convection can grow once a lifting mechanism is provided. In the previous six hours, deep moist convection is suppressed by the thermal inversion, permitting the generation of the urban boundary layer.

The environmental wind profile is defined by the quarter-circle hodograph proposed by Rotunno and Klemp (1982). The profiles of the zonal $u(z)$ and meridional $v(z)$ wind components used for the current study, and plotted in the hodograph of Figure 1a, are defined as:

$$u(z) = \begin{cases} u_1 - u_1 cos\left(\frac{\pi z}{2h_1}\right) - \frac{u_2}{4} & z < h_1 \\ u_1 + (z - h_1)\frac{u_2 - u_1}{h_2 - h_1} - \frac{u_2}{4} & h_1 \leq z < h_2 \\ \frac{3}{4}u_2 & z \geq h_2 \end{cases} \tag{3}$$

and

$$v(z) = \begin{cases} v_1 sin\left(\frac{\pi z}{2h_1}\right) & z < h_1 \\ v_1 & z \geq h_1 \end{cases} \tag{4}$$

where $h_1 = 1500$ m, $h_2 = 6000$ m, $u_1 = 7$ m s^{-1}, $u_2 = 40$ m s^{-1}, $v_1 = 10$ m s^{-1} are chosen to produce a right-mover supercell (Markowski and Dotzek 2011 used similar parameters). The diurnal mixing in the boundary layer changes the imposed wind profiles, as can be inferred by comparing the hodographs at 10:00 am and 04:00 pm in Figure 1. This is also a consequence of the lack of a meridional thermal gradient in the domain, which hinders the presence of a thermal wind capable of maintaining the curved hodograph in long-lasting simulations.

The transient evolution of the simulated profile suggests that the optimal timing for triggering the supercell should be carefully estimated. The first hours of the simulations are spin-up time, where the radiative heating grows the PBL. In this first phase, thermodynamic and kinematic atmospheric parameters change (as shown in Figure S1); in particular, CAPE and LCL increase, Convective Inhibition (CIN) and Storm Relative Helicity (SRH) decrease. Between 5:00 pm and 8:00 pm, these parameters reach a minimum and a quasi-steady state, before nocturnal radiative cooling again significantly modifies the atmosphere. Therefore, triggering the storm at 04:00 pm and analyzing its interaction with the urban area between 05:00 pm and 07:00 pm is an appropriate choice. Any modifications observed in the numerical experiments in that timespan can be attributed to the urban morphological parameters rather than to changes in the broader environment.

Values of some relevant parameters computed on the simulated sounding at 04:00 pm, when convection is initiated, are shown in Table 1. At 04:00 pm, the atmosphere is conducive to supercell storms, since the substantial—albeit not extreme—CAPE (2740 J kg^{-1}), strong bulk shear 0-6 km (32.3 m s^{-1}) and moderate SRH (200 J kg^{-1}).

2.3 The numerical experiments

The BEP-BEM model requires several urban morphological parameters to run. The thermal features of the city are kept constant: the default values (reported in Table 2) of Local Climate Zone 2 are used (Ching et al., 2018). The sensitivity of the supercell to some of them is investigated in this work: street width (s), building width (b), building height (h_b), and urban fraction (*uf*). In Table 3, a summary of the numerical experiments conducted is provided, while in Figure 2, a graphical summary is furnished. The range of parameters explored is selected by studying the mean morphological parameters of some European

Acronym	Index	Value
CAPE	convective available potential energy	2740 J kg^{-1}
CIN	convective inhibition	0 J kg^{-1}
bulk shear 0- 6 km	bulk shear 0-6 km	32.3 m s^{-1}
SRH 0-3 km	storm relative helicity in the 0-3 km layer	200 J kg^{-1}
SRH 0-1 km	storm relative helicity in the 0-1 km layer	33 J kg^{-1}

Table 1. Some relevant thermodynamic and kinematic indices computed on the simulated sounding at 04:00 pm shown in Figure 1b.

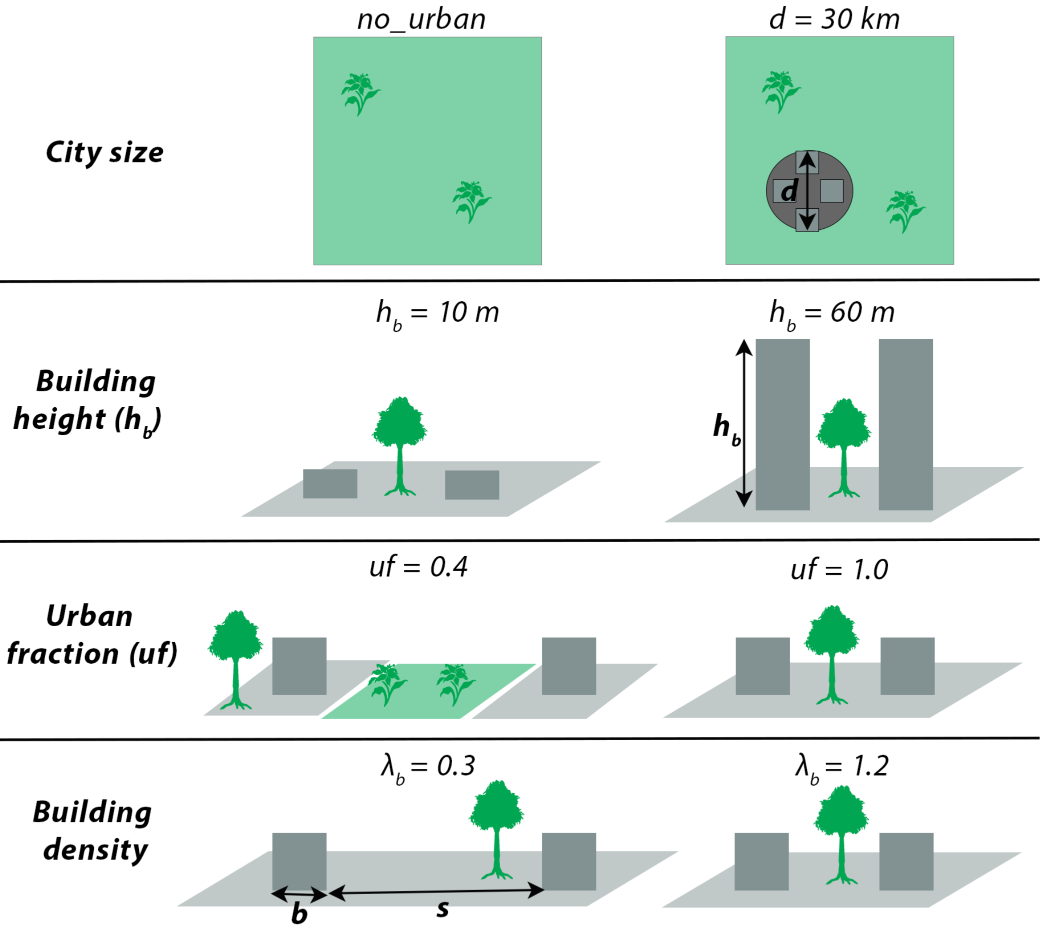

Figure 2. Schematic representation of some of the urban features explored in the idealized simulations. The *zero value* (left) and the *max value* (right) of the studied urban morphological parameters (city size, building height, urban fraction, and building density) are shown (see Table 3). In the first row, the simulation domain is depicted from above, showing croplands (green shading with plants) and the city (grey circle). In the remaining rows, the view is lateral. Grey rectangles represent buildings. d denotes the city diameter, h_b the building height, uf the urban fraction, s the street width, b the building width, and λ_b the ratio of building area to total area.

	Heat Capacity ($\mathrm{Jm^{-3}K^{-1}}$)	Thermal Conductivity ($\mathrm{Jm^{-1}s^{-1}K^{-1}}$)	Surface Albedo	Surface Emissivity
Ground	1.68×10^6	0.73	0.14	0.95
Walls	1.67×10^6	1.09	0.3	0.90
Roofs	1.8×10^6	1.25	0.3	0.91

Table 2. Thermal features of the idealized city.

numerical experiments	zero value	intermediate values	max value
city size 1 (km)	0 (no_urban)	5; 10; 15; 20; 25	30
city size 2 (km)	0 (no_urban)	5; 10; 15; 20; 25	30
urban fraction	0.4	0.6; 0.8	1.0
building height (m)	10	20; 40	60
building density (λ_p, λ_b)	(0.1,0.3)	(0.2, 0.6) ; (0.3,0.9)	(0.4,1.2)
green roofs	no_urban		green roofs over all roofs
no_thermo	no_urban		buildings with rural energetic balance
NYC	no_urban		NYC parameters
bubble	no_urban		bubble shifted from (40,40) to (30,60)

Table 3. Numerical experiments conducted and parameters explored.

and US cities frequently affected by severe storms (see, for example, Table S1 and Figure S2), using the GLobal Building heights for Urban Studies (GLOBUS) dataset (Kamath et al., 2024). In that dataset, the plan area fraction (λ_p) and the building surface-to-plan area ratio (λ_b) are reported. These are defined as:

$$\lambda_p = \frac{b}{s+b} \tag{5}$$

$$\lambda_b = \frac{2h_b}{s+b} + \lambda_p. \tag{6}$$

First, a sensitivity analysis of city size is conducted, with city diameters ranging from 0 km in the *no_urban* scenario to 30 km (numerical experiments *city size 1*). Table 4 presents the parameters used to define the idealized city uniformly in the numerical experiments *city size 1*. These are based on the Milan GLOBUS data (Table S1). Milan is chosen as the reference city both because it was object of investigation in a preceding case study analysis (De Martin et al., 2025), and also because its morphological parameters are relatively typical of European cities.

	no_urban	*5km_1*	*10km_1*	*15km_1*	*20km_1*	*25km_1*	*30km_1*
city diameter (km)	0	5	10	15	20	25	30
urban fraction	0.63	0.63	0.63	0.63	0.63	0.63	0.63
building height (m)	20	20	20	20	20	20	20
λ_p	0.24	0.24	0.24	0.24	0.24	0.24	0.24
λ_b	0.78	0.78	0.78	0.78	0.78	0.78	0.78

Table 4. Urban morphological parameters used in the set of numerical experiments *city size 1* (in the first row the name of the experiments is reported).

	no_urban	*5km_2*	*10km_2*	*15km_2*	*20km_2*	*25km_2*	*30km_2*
city diameter (km)	0	5	10	15	20	25	30
urban fraction	1.0	1.0	1.0	1.0	1.0	1.0	1.0
building height (m)	20	20	20	20	20	20	20
λ_p	0.24	0.24	0.24	0.24	0.24	0.24	0.24
λ_b	0.78	0.78	0.78	0.78	0.78	0.78	0.78

Table 5. As in Table 4, but for numerical experiments *city size 2*.

The same set of numerical experiments is also performed using an urban fraction of 1.0 instead of 0.63 (numerical experiments *city size 2*, Table 5). An urban fraction of 1.0 means the entire urban surface is built-up (i.e., no croplands within the city radius). However, 20% of the street surface remains covered by trees in these experiments, as a city without any trees is unrealistic. Although a mean urban fraction of 1.0 is not observed in European or U.S. cities (Table S1), this experiment is conducted to explore the impact of city size under the extreme scenario of a fully urbanized city.

	uf0.4	*uf0.6*	*uf0.8*	*uf1.0*
city diameter (km)	20	20	20	20
urban fraction	0.4	0.6	0.8	1.0
building height (m)	20	20	20	20
λ_p	0.24	0.24	0.24	0.24
λ_b	0.78	0.78	0.78	0.78

Table 6. As in Table 4, but for numerical experiments *urban fraction* (uf).

	h10	*h20*	*h40*	*h60*
city diameter (km)	20	20	20	20
urban fraction	0.63	0.63	0.63	0.63
building height (m)	10	20	40	60
λ_p	0.24	0.24	0.24	0.24
λ_b	0.78	0.78	0.78	0.78

Table 7. As in Table 4, but for numerical experiments *building height* (h_b).

	λ_b*0.3*	λ_b*0.6*	λ_b*0.9*	λ_b*1.2*
city diameter (km)	20	20	20	20
urban fraction	0.63	0.63	0.63	0.63
building height (m)	20	20	20	20
λ_p	0.1	0.2	0.3	0.4
λ_b	0.3	0.6	0.9	1.2

Table 8. As in Table 4 but for numerical experiments *building density*.

A third set of numerical experiments, called *urban fraction*, is conducted to examine the supercell's sensitivity to urban fraction. Values ranging from 0.4 to 1.0 are investigated for an idealized city with a diameter of 20 km (Table 6).

The *building height* experiments, investigate the effect of building height on the simulated storm (Table 7). The building heights explored range from 10 to 60 m, representing cities from the Chicago metropolitan area to downtown New York.

Furthermore, the *building density* experiments, explore the effect of building density on the simulated storms (Table 8). Since the BEP-BEM scheme uses street and building widths as input parameters (rather than the λ parameters), the building height and the building width are kept constant at 20 m, while the street width is varied from 106 m to 11.5 m. This corresponds to a range of (λ_p, λ_b) values from (0.1, 0.3) to (0.4, 1.2), representing a transition from a very dispersed to a highly compact city.

Lastly, some additional experiments are conducted to investigate other specific questions. An experiment is carried out using the settings of numerical experiment *30km_2*, but with vegetation placed over all the buildings of the idealized city (Zonato et al., 2021), to investigate the effect of this nature-based solution on storm dynamics (this experiment is called *green roofs*; see Table 3). A second experiment, called *no_thermo*, is conducted with the settings of the *30km_2* experiment and the same urban roughness, but with the urban energetic balance replaced by the rural one. This experiment serves to disentangle the dynamical and thermodynamical effects of the city on storm dynamics and the pre-storm environment. Another experiment, called *NYC* (Table 3), is run to test the hypothesis of storm bifurcation caused by the building barrier effect, first proposed by Bornstein and Lin (2000) for New York City (NYC). This experiment is run using a city diameter of 8 km and the same parameters of downtown NYC shown in Table S1. An experiment, called *bubble* (Table 3), is also run to test the sensitivity of the urban-induced storm modification to the storm trajectory. In this experiment, the thermal bubble is shifted from grid-point (40,40) to (30,60), while keeping the same parameters of experiment *30km_2* (Table 5).

2.4 Generation of the ensembles

An ensemble approach is adopted to better assess the physical signal of urban-induced storm modifications across different flow realizations, given the intrinsic chaotic variability of the atmosphere. For each numerical experiment, eleven simulations are conducted: one is the control run, and the other ten are generated using the Stochastic Kinetic Energy Backscatter Scheme (SKEBS, Berner et al. 2009. In the present study, the parameters used to generate the ensemble with SKEBS are set following Romine et al. (2014), who investigated ensemble dispersion in deep moist convective events. The only difference from their setup is the value of the maximum wavenumber, which is set to match the number of grid points in the current simulations.

The ten ensemble members are generated using ten distinct random seeds, which are kept constant across all numerical experiments. As a result, the same members across different experiments are using the same seeds and are not fully independent (this is considered in the statistical analysis). This is done intentionally to better evaluate the influence of each parameter over the different flow evolutions (i.e., members).

2.5 Storm tracking

The Statistical and Programmable Objective Updraft Tracker (SPOUT, Terwey and Rozoff 2014) algorithm is used to track the simulated updrafts. Fine-tuning of some user-defined parameters is necessary to achieve satisfactory tracking of the supercell updrafts. Table S2 lists these parameters and compares them with those originally employed by Terwey and Rozoff (2014).

Further filtering of the SPOUT-detected tracks is necessary to isolate the supercell track, as the algorithm frequently splits it. This occurs because SPOUT tracks updrafts individually, and supercells may cycle, producing new updrafts. Additionally, other storms are triggered in the simulations due to the left-moving supercell.

To filter out these updrafts, only the track that begins near the location where the thermal bubble is released is considered. If the track terminates at $x < 150$ (i.e., before three hours after the bubble release), a new track is searched for within a 10 km radius. If found, the new track is connected to the previous one. This process is repeated until the track reaches $x = 150$ or the storm dissipates. An example of the eleven tracks obtained for the eleven ensemble members using this tracking algorithm is shown in Figure S3.

Each point along the track is considered the storm center at a given time step. Storm diagnostics are extracted every 10 minutes, and the extracted variables are listed in Table 9. For each time step, the mean (or maximum or minimum, depending on the variable) is calculated within an 8-km radius around the storm center, and this value is assigned to the storm at that time step.

Then, three regions are defined using a temporal criterion to compare the storms at the same developmental stage across different numerical experiments. Those regions are defined with respect to a zero, defined as the time step when the supercell is above the city, corresponding to grid point (90,76) in the control run of the *no_urban* experiment. This time step is at 06:00

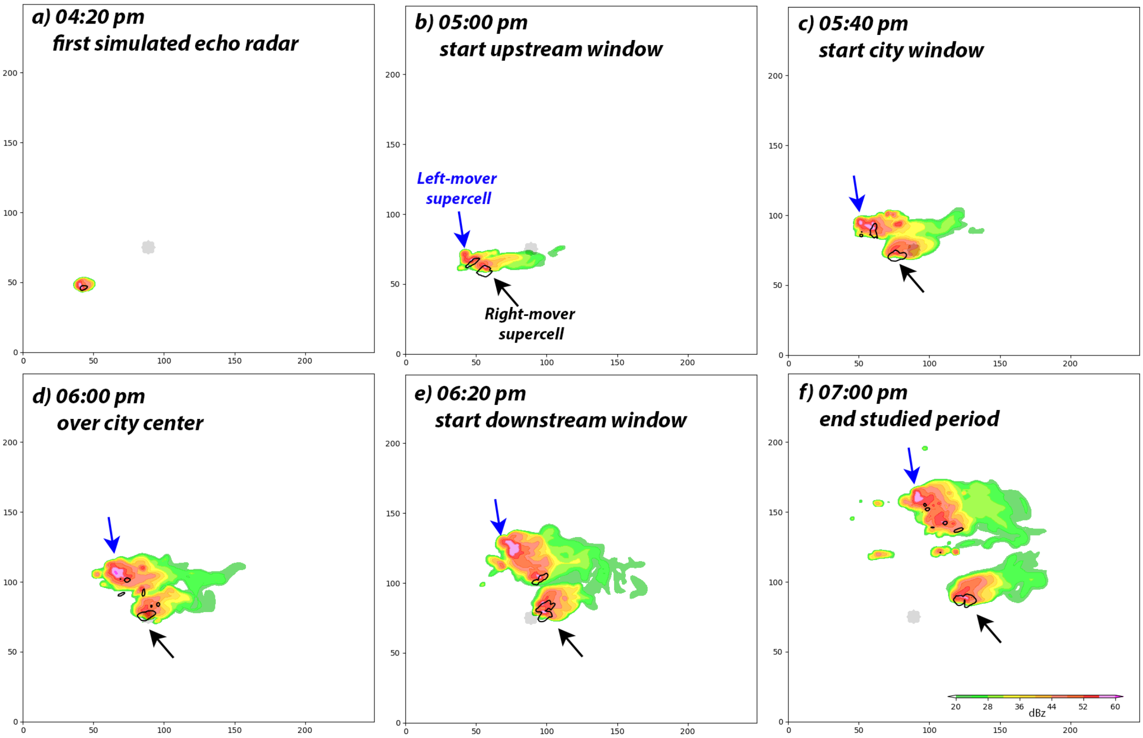

Figure 3. Maximum simulated reflectivity (colour shading) at a) 04:20 pm, b) 05:00 pm, c) 05:40 pm, d) 06:00 pm, e) 06:20 pm, f) 07:00 pm by the control run of numerical experiment *10km_1*. The city is shown with a grey shading. UH value higher than 100 m s^{-1} are highlighted with a black contour. The black (blue) arrow indicates the right-mover (left-mover) supercell.

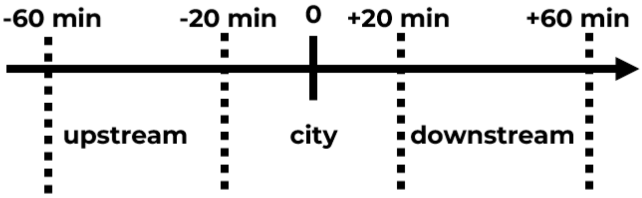

Figure 4. Criterion used to define the upstream, city and downstream regions.

pm (see, for instance, Fig. 3d). Then, three 40-minute windows are defined (sketch in Figure 4). The first one, from -20 to + 20 minutes, defines the *city region*. The *upstream region* is defined from -60 to -20 minutes. Lastly, the *downstream region* is defined from +20 minutes to +60 minutes. In these windows, the variables previously computed for each time step are averaged. Thus, considering the 10-minute output frequency, four time steps are averaged for each window.

https://doi.org/10.5194/egusphere-2026-815
Preprint. Discussion started: 23 February 2026

2.6 Statistical method used to analyze the numerical experiments

Given a set of numerical experiments, a statistical analysis is conducted for each region and for each variable. The variables are normalized with respect to a reference zero value (defined case-by-case in Table 3). The normalized z_{ij} variable for the ensemble member j and numerical experiment i is given by:

$$z_{ij} = \frac{x_{ij} - x_{0j}}{x_{0j}} \tag{7}$$

where x_{ij} is the original variable and x_{0j} is the reference value for the ensemble member j. This approach is adopted because the interest is in understanding how storm diagnostics vary relative to a reference case (e.g., how updraft speed changes with increasing city size compared to the *no_urban* case). A linear fit is performed using the *curve_fit* function from SciPy (Virtanen et al., 2020) on the normalized variables sharing the same SKEBS seed. Any null values are excluded: specifically, if a storm dissipates, the corresponding ensemble member is omitted from the fit. This exclusion is necessary because, for some variables (e.g., Θ), including a null value in the linear fit lacks physical meaning. In general, excluding such values has been observed to increase the fit's statistical significance.

We focus solely on the slope parameter of the linear fit, particularly its sign. The statistical significance of the slope relative to a null hypothesis of a zero slope is assessed using a 5–95% bootstrap confidence interval, computed from 1000 iterations using the *bootstrap* function of SciPy.

3 Results: Supercell sensitivity to the urban morphological parameters

In this section, the sensitivity of the simulated supercell to urban morphological parameters is presented. Across the different ensemble members, there are variations in the storm tracks and intensity; however, all simulations of the *no_urban* reference experiment produce a long-lasting, right-moving supercell, similar to the one shown in Fig. 3 for the *10km_1* experiment. The right-mover supercell approaches the city from the WSW (Fig. 3c) and remains isolated and intense also one hour after hitting the city (Fig. 3f).

3.1 *City size*

In the numerical experiments *city size 1*, the effect of increasing the diameter of the city with the same characteristics as Milan on the supercell is investigated. The normalized mean value of the storm's UH in the *city region* is shown in Fig. 5a for each ensemble member as a function of city diameter (the same plots for the *upstream* and *downstream regions* are displayed in Figure S4). In the *city region*, there is a clear decreasing trend in UH, even with considerable ensemble spread. A similar pattern is observed in the *upstream region* (Fig. S4a), whereas in the *downstream region* a more consistent decreasing trend is seen across all ensemble members (Fig. S4c).

https://doi.org/10.5194/egusphere-2026-815
Preprint. Discussion started: 23 February 2026

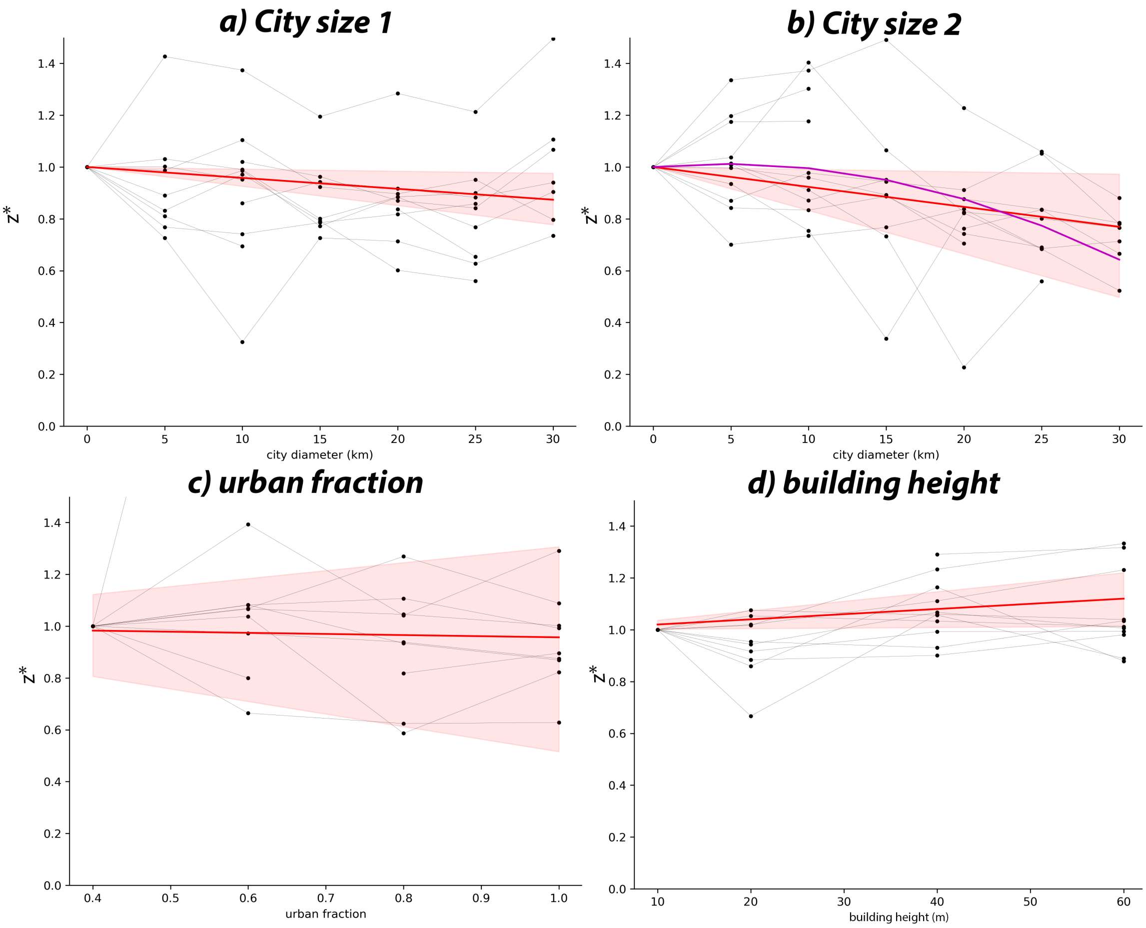

Figure 5. a) Normalized mean UH (z*) in each ensemble member (black dots) of the *city size 1* set of experiments (Table 4) in function of the city diameter (km) in the *city region*. Ensemble members obtained with the same seed are connected. The mean linear fit is shown with a red line, while the 5-95% confidence interval is red shaded. b), c) and d) as in a) but for the *city size 2*, *urban fraction* and *building height* set of experiments, respectively. In b), a quadratic fit is shown with a purple line.

Table 9 presents the mean slopes for each storm diagnostic variable in the three regions. A general negative trend is observed, though it is statistically significant (the trends are statistically significant lower than zero) only for some of them[2]. The trend is particularly significant in the *city region* and for the vertical velocity and vorticity at 500 hPa, and for UH. This indicates that the supercell weakens as city diameter increases, with the weakening more pronounced and statistically significant lower than zero at the mid-levels and when the storm is over the city. The increasing trend shown by some ensemble members in Fig. S4a and 5a suggests that, even if rare, an intensification of the supercell is possible in the *upstream* and *city regions*[3].

variable	meaning	upstream	city	downstream
wmax	maximum vertical velocity	-2.6×10^{-3}	-2.1×10^{-3}	-1.1×10^{-3}
w500	maximum vertical velocity at 500 hPa	$\mathbf{-6.1\times10^{-3}}$	$\mathbf{-3.1\times10^{-3}}$	-1.8×10^{-3}
ζ 500	maximum vertical vorticity at 500 hPa	$\mathbf{-3.9\times10^{-3}}$	$\mathbf{-2.0\times10^{-3}}$	$\mathbf{-2.6\times10^{-3}}$
uh max	maximum updraft helicity	$\mathbf{-3.1\times10^{-3}}$	$\mathbf{-4.6\times10^{-3}}$	-3.7×10^{-4}
uh mean	mean updraft helicity	-3.3×10^{-3}	$\mathbf{-4.2\times10^{-3}}$	$\mathbf{-5.7\times10^{-3}}$
w700	maximum vertical velocity at 700 hPa	$\mathbf{-1.4\times10^{-3}}$	$\mathbf{-1.9\times10^{-3}}$	-2.8×10^{-4}
ζ 700	maximum vertical vorticity at 700 hPa	$+3.8\times10^{-4}$	-8.7×10^{-4}	-6.5×10^{-4}
w850	maximum vertical velocity at 850 hPa	$\mathbf{-1.3\times10^{-3}}$	$\mathbf{-3.6\times10^{-3}}$	-2.0×10^{-3}
ζ 850 max	maximum vertical vorticity at 850 hPa	-1.5×10^{-4}	$+2.1\times10^{-4}$	-5.7×10^{-4}
w950	maximum vertical velocity at 950 hPa	$+2.1\times10^{-5}$	$\mathbf{-5.4\times10^{-3}}$	$\mathbf{-3.7\times10^{-3}}$
ζ 950	maximum vertical vorticity at 950 hPa	-7.8×10^{-4}	-2.6×10^{-3}	$\mathbf{-5.1\times10^{-3}}$
Θ_e(500 hPa) max	maximum equivalent potential temperature at 500 hPa	-6.3×10^{-5}	$\mathbf{-1.9\times10^{-4}}$	-7.1×10^{-6}
Θ_e(500 hPa) mean	mean equivalent potential temperature at 500 hPa	$\mathbf{-3.7\times10^{-5}}$	-3.4×10^{-5}	-1.2×10^{-5}
Θ(5 m) min	minimum potential temperature in the first model level	-2.9×10^{-5}	$+5.4\times10^{-5}$	$\mathbf{+8.1\times10^{-5}}$
Θ(5 m) mean	mean potential temperature in the first model level	-1.6×10^{-5}	$\mathbf{+4.9\times10^{-5}}$	$+2.1\times10^{-5}$

Table 9. List of storm diagnostic variables used (every value is computed considering an 8-km radius following the storm track) and corresponding mean slopes (km^{-1}) of the linear fits between diagnostic variables and city diameters in the *city size 1* numerical experiments. Bold values are statistically significant lower (or larger) than zero.

In the *city size 2* experiments, a similar trend of the *city size 1* sample is observed, but the weakening of the storm is even more pronounced (Fig. 5b). This weakening is particularly evident downstream of the city and, in this case, is statistically significant lower than zero also for several low-level storm diagnostic variables (Table 10)[4]. In the *city region*, a quadratic fit is statistically significant lower than zero (purple line in Fig. 5b). For city diameters up to about 10 km, the city has little effect on the storm. However, in larger cities, the storm weakens faster with city size than a linear fit would suggest.

---

[2] Θ shows a positive trend. This is because the cold pools weaken as the storm weakens, leading to less pronounced negative Θ anomalies associated with downdrafts—i.e., a relative increase in Θ.

[3] This occurs when there is a coincidental weakening of the storm in the no-urban simulations.

[4] Note, however, that a positive trend in vertical vorticity at 850 and 700 hPa is observed in the *city region*, with statistical significance at 850 hPa.

The cumulative ensemble mean of UH clearly illustrates the effect of urban land use on the supercell. In the *no_urban* experiment, a substantial UH swath is present (Fig. 6a), which is considerably weakened as it passes over the city (Fig. 6b). The suppression becomes nearly complete in the *30km_2* experiment (Fig. 6c). Notably, the suppression is significantly more pronounced in the *city size 2* sample than in the *city size 1* sample (Fig. 6d). When the bubble is shifted northward in the *bubble* experiment (described in Table 3), the weakening of the supercell occurs even more rapidly than in the *30km_2* experiment (Figure S5).

variable	upstream (*size2*)	city (*size2*)	downstream (*size2*)	upstream (*uf*)	city (*uf*)	downstream (*uf*)
wmax	$\mathbf{-3.9 \times 10^{-3}}$	-3.7×10^{-3}	$\mathbf{-3.7 \times 10^{-3}}$	$\mathbf{-4.1 \times 10^{-2}}$	-8.6×10^{-2}	-1.2×10^{-1}
w500	$\mathbf{-8.1 \times 10^{-3}}$	-8.7×10^{-3}	$\mathbf{-4.1 \times 10^{-3}}$	$\mathbf{-4.8 \times 10^{-2}}$	-1.6×10^{-1}	-1.8×10^{-1}
ζ 500	$\mathbf{-4.8 \times 10^{-3}}$	$\mathbf{-4.3 \times 10^{-3}}$	$\mathbf{-4.3 \times 10^{-2}}$	$\mathbf{-3.6 \times 10^{-2}}$	-7.6×10^{-2}	-7.5×10^{-2}
uh max	$\mathbf{-4.1 \times 10^{-3}}$	$\mathbf{-6.8 \times 10^{-3}}$	3.3×10^{-3}	-2.7×10^{-2}	-1.0×10^{-1}	-1.9×10^{-1}
uh mean	$\mathbf{-6.4 \times 10^{-3}}$	$\mathbf{-7.7 \times 10^{-3}}$	$\mathbf{-9.7 \times 10^{-3}}$	$\mathbf{-4.9 \times 10^{-2}}$	-4.3×10^{-2}	-2.6×10^{-1}
w700	-1.8×10^{-3}	-1.8×10^{-3}	$\mathbf{-3.1 \times 10^{-3}}$	-1.8×10^{-2}	-1.2×10^{-1}	-1.1×10^{-1}
ζ 700	-7.8×10^{-4}	$+3.45 \times 10^{-5}$	$\mathbf{-2.7 \times 10^{-3}}$	-5.8×10^{-3}	-3.4×10^{-3}	-1.6×10^{-3}
w850	$\mathbf{-2.4 \times 10^{-3}}$	$\mathbf{-4.3 \times 10^{-3}}$	$\mathbf{-3.4 \times 10^{-3}}$	$+5.0 \times 10^{-3}$	-7.2×10^{-2}	-8.7×10^{-2}
ζ 850	-8.1×10^{-4}	$\mathbf{+7.1 \times 10^{-4}}$	$\mathbf{-7.2 \times 10^{-3}}$	$\mathbf{+2.2 \times 10^{-2}}$	-5.5×10^{-2}	$+1.1 \times 10^{-1}$
w950	-9.1×10^{-4}	$\mathbf{-6.1 \times 10^{-3}}$	$\mathbf{-5.6 \times 10^{-3}}$	-5.1×10^{-4}	$+1.4 \times 10^{-2}$	-1.1×10^{-1}
ζ 950	$+6.6 \times 10^{-4}$	$\mathbf{-4.7 \times 10^{-3}}$	$\mathbf{-3.7 \times 10^{-3}}$	-1.6×10^{-3}	-2.8×10^{-2}	-1.8×10^{-1}
$\Theta_e(500\,\mathrm{hPa})$ max	$\mathbf{-2.6 \times 10^{-2}}$	$\mathbf{-2.4 \times 10^{-4}}$	-1.3×10^{-4}	-1.0×10^{-3}	-6.3×10^{-3}	-5.9×10^{-3}
$\Theta_e(500\,\mathrm{hPa})$ mean	$\mathbf{-9.6 \times 10^{-5}}$	-5.5×10^{-5}	$\mathbf{-7.1 \times 10^{-5}}$	-2.8×10^{-4}	-1.7×10^{-3}	$\mathbf{-3.7 \times 10^{-3}}$
$\Theta(5\,\mathrm{m})$ min	-8.9×10^{-7}	$\mathbf{+1.1 \times 10^{-4}}$	$\mathbf{+1.7 \times 10^{-4}}$	-3.1×10^{-4}	$+4.0 \times 10^{-4}$	$+1.2 \times 10^{-3}$
$\Theta(5\,\mathrm{m})$ mean	-1.0×10^{-5}	$\mathbf{+7.5 \times 10^{-5}}$	$\mathbf{+7.2 \times 10^{-5}}$	-3.7×10^{-5}	$+3.4 \times 10^{-4}$	$+5.0 \times 10^{-4}$

Table 10. Slope of fitting lines between diagnostic variables of the supercell and *city size 2* experiments (*size 2*, left block, units m^{-1}), or urban fraction (*uf*, right block). Bolded values are statistically significant lower (or larger) than zero.

A particularly interesting feature in the *30km_2* experiment is the emergence of a new UH swath north of the city (Fig. 6c). To better understand this behavior, the same time steps showing maximum reflectivity from ensemble member 1 of the *30km_2* experiment (Fig. 7) are compared with those from the control run of the *10km_1* experiment (Fig. 3). In the *30km_2* experiment, the initial supercell is suppressed very early, already by 05:00 pm (Fig. 7b). However, a stripe of vertical velocities exceeding $0.5\ \mathrm{ms}^{-1}$ extends from the city toward the northwest. Just east of this stripe, new convective cells begin to develop between 05:40 pm (Fig. 7c) and 06:20 pm (Fig. 7e). By 07:00 pm, a new right-moving supercell forms from these earlier convective initiations (Fig. 7f). Thus, in this simulation, the original supercell is suppressed, while a new, urban-induced supercell develops. This behavior occurs in 8 out of 11 members of the *30km_2* experiment and is not observed in any of the other experiments (see Figs. 6 and 8). Additional evidence supporting the urban origin of the second supercell initiated at 07:00 pm will be presented in Section 4.

https://doi.org/10.5194/egusphere-2026-815
Preprint. Discussion started: 23 February 2026

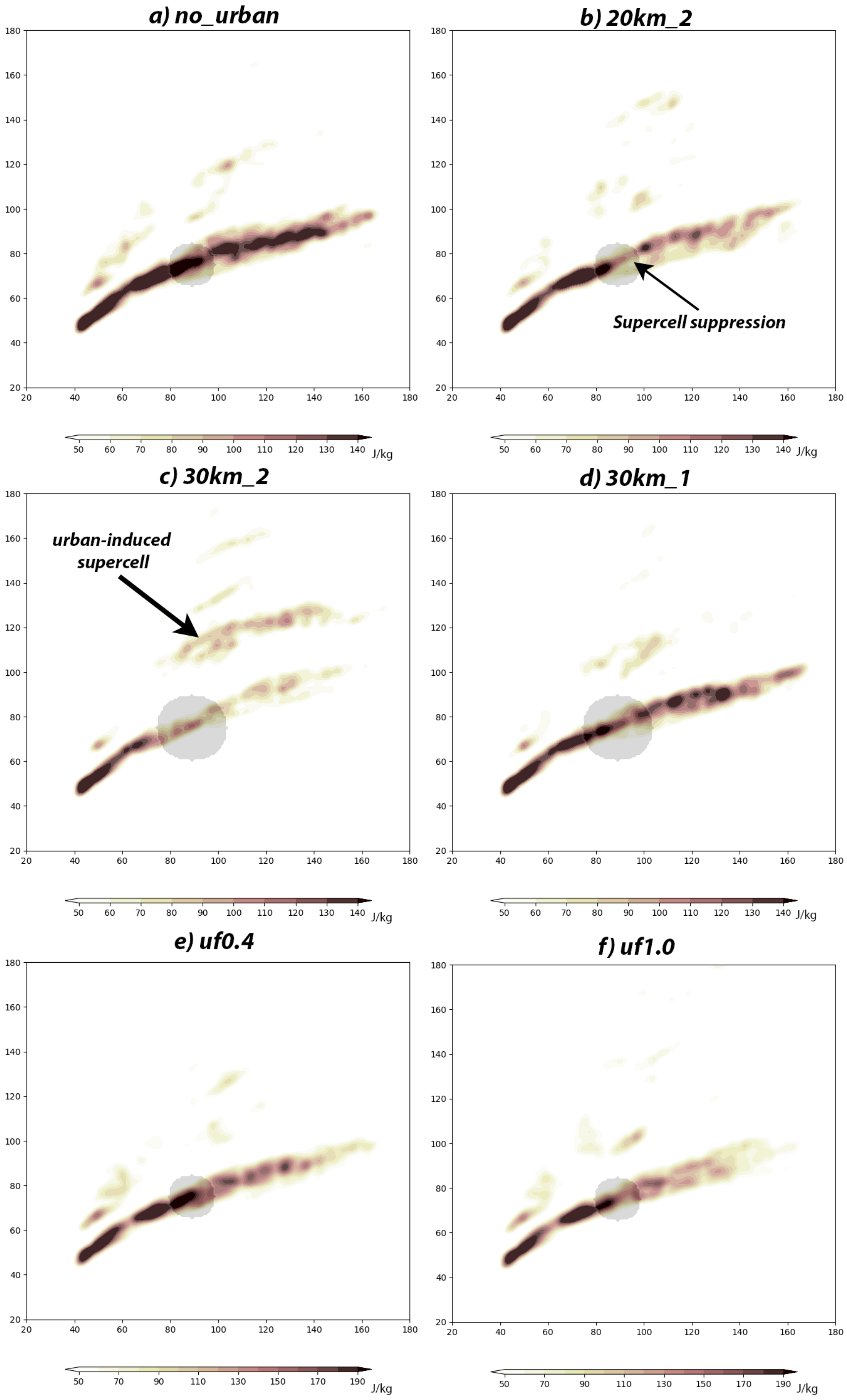

Figure 6. Cumulated UH ensemble mean in a) the *no_urban* experiment (Table 5), b) in the *20km_2* experiment, c) in the *30km_2* experiment, d) in the *30km_1* experiment (Table 4), e) in the *uf0.4* experiment (Table 6), f) in the *uf1.0* experiment. The city is highlighted in grey shading. In a) the city of the *20km* experiment is shown just for reference, in the experiment there are croplands everywhere.

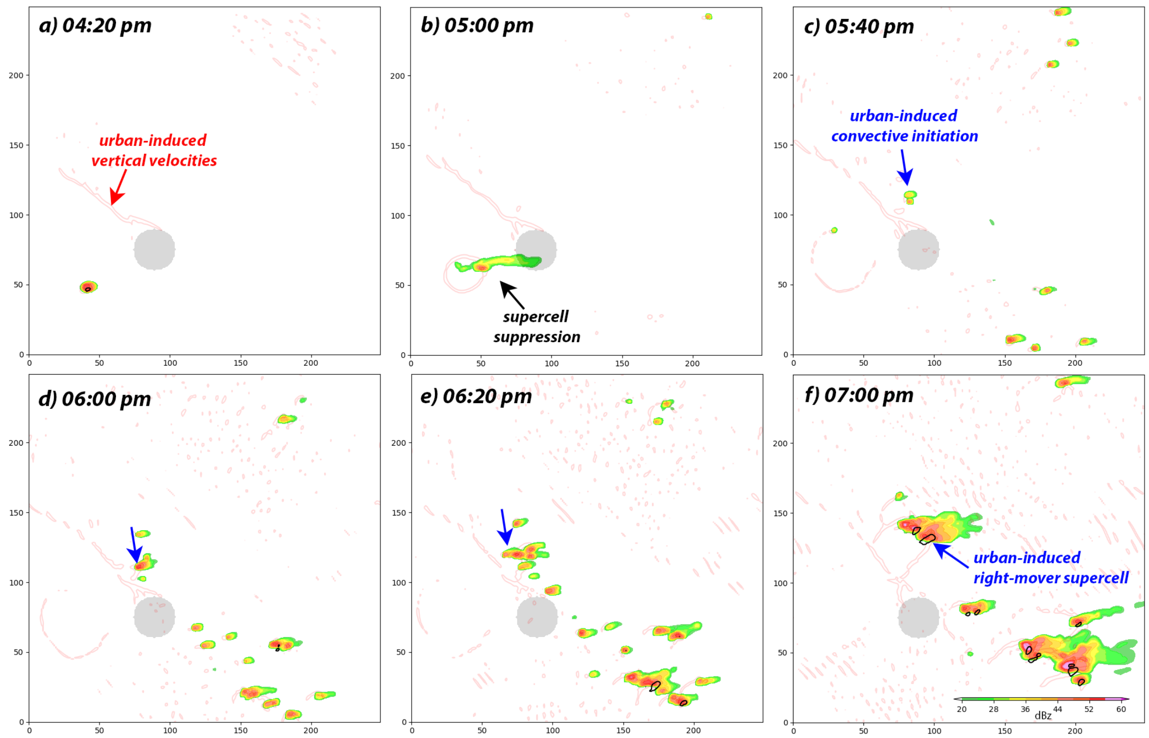

Figure 7. As in Fig. 3, but for the ensemble member 1 of the *30km_2* numerical experiment. Vertical velocities at 950 hPa higher than 0.5 m s^{-1} are plotted with red contours. The blue arrows indicate the triggering of the urban-induced right-mover supercell.

3.2 Urban fraction

In the *urban fraction* experiments, most storm diagnostic variables decrease as a function of the urban fraction (Table 10). However, only some of these trends are statistically significant lower than zero in the *upstream region*. By contrast, no statistically significant trends are observed in the *city* and *downstream regions* (except for Θ_e(500 hPa) in the *downstream regions*). In the *upstream region*, the ensemble spread is relatively small (Fig. S6a), which leads to statistically significant trends—even though the slope of the mean linear fit is smaller than in the other two regions. Nevertheless, examining the ensemble mean of the UH swath in the *uf0.4* and *uf1.0* experiments (Figure 6e,f) reveals a visible weakening of the storm. We conclude that the supercell weakens with increasing urban fraction, although this trend is not statistically significant lower than zero.

3.3 Building height

An opposite trend is observed in the supercell's sensitivity to building height. In all three regions, the mean UH increases with increasing building height (Fig. 5d and S6). The positive trend in mean UH is statistically significant larger than zero across all three regions studied (Table 11). Other mid-level storm diagnostic variables exhibit a similar positive trend; however, these trends are statistically significant larger than zero only in the *upstream* and *city regions* for some variables (e.g., w500 and

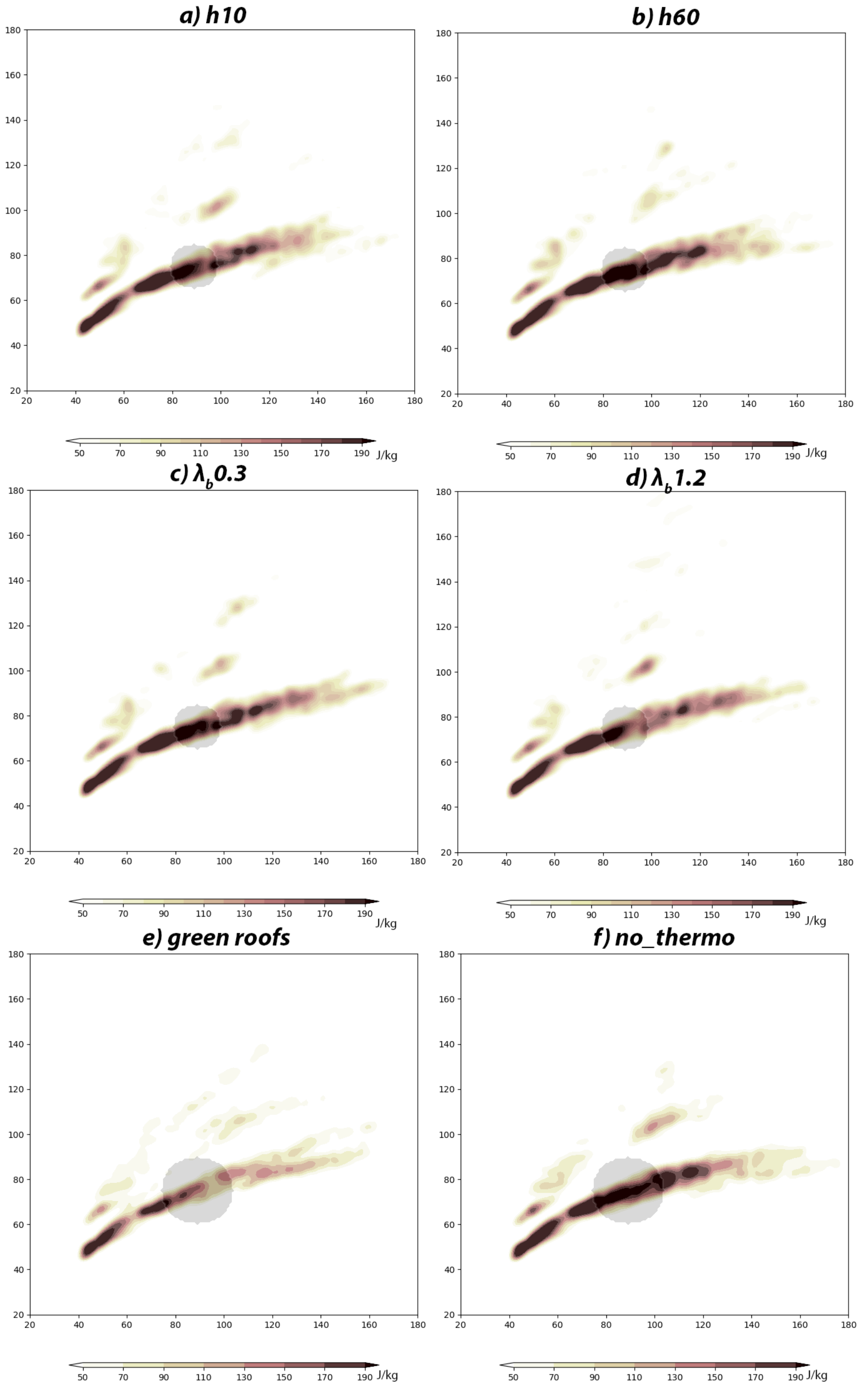

Figure 8. As in Fig. 6, but for a) *h10* experiment (Table 7), b) *h60* experiment, c) $\lambda_b 0.3$ experiment (Table 7), d) $\lambda_b 1.2$ experiment, e) *green roofs* experiment (Table 3) and f) *no_thermo* experiment (Table 3).

variable	upstream (h_b)	city (h_b)	downstream (h_b)	upstream (λ_b)	city (λ_b)	downstream (λ_b)
wmax	$\mathbf{+6.8 \times 10^{-4}}$	$\mathbf{+9.4 \times 10^{-4}}$	$+1.3 \times 10^{-3}$	$\mathbf{-1.2 \times 10^{-2}}$	-3.5×10^{-2}	$+2.1 \times 10^{-3}$
w500	$\mathbf{+8.0 \times 10^{-4}}$	$\mathbf{+8.6 \times 10^{-4}}$	$+1.1 \times 10^{-3}$	$\mathbf{-8.0 \times 10^{-3}}$	-4.3×10^{-2}	$+7.5 \times 10^{-3}$
ζ 500	$\mathbf{+8.1 \times 10^{-4}}$	$+3.2 \times 10^{-4}$	-1.2×10^{-3}	$\mathbf{-1.6 \times 10^{-2}}$	-2.2×10^{-2}	-3.8×10^{-2}
uh max	$+5.2 \times 10^{-4}$	$\mathbf{+1.8 \times 10^{-3}}$	$+7.7 \times 10^{-4}$	-1.1×10^{-2}	$\mathbf{-3.8 \times 10^{-2}}$	$+4.6 \times 10^{-2}$
uh mean	$\mathbf{+5.1 \times 10^{-3}}$	$\mathbf{+2.0 \times 10^{-3}}$	$\mathbf{+6.3 \times 10^{-3}}$	-9.2×10^{-3}	-6.2×10^{-2}	$+5.4 \times 10^{-2}$
w700	$\mathbf{+3.2 \times 10^{-4}}$	$\mathbf{+6.3 \times 10^{-4}}$	$+3.7 \times 10^{-4}$	-9.2×10^{-4}	$\mathbf{-3.4 \times 10^{-2}}$	$+1.9 \times 10^{-2}$
ζ 700	$+5.0 \times 10^{-5}$	-8.1×10^{-4}	-9.0×10^{-4}	$+4.3 \times 10^{-3}$	$+1.1 \times 10^{-2}$	$+7.4 \times 10^{-3}$
w850	-4.6×10^{-5}	-2.7×10^{-4}	-4.1×10^{-4}	$+2.9 \times 10^{-3}$	-1.8×10^{-2}	-2.1×10^{-3}
ζ 850	-5.6×10^{-4}	$+6.6 \times 10^{-5}$	-1.4×10^{-3}	$+2.2 \times 10^{-2}$	-3.2×10^{-2}	$+1.0 \times 10^{-1}$
w950	$\mathbf{+2.1 \times 10^{-4}}$	$\mathbf{-3.2 \times 10^{-3}}$	-2.2×10^{-3}	$\mathbf{-1.1 \times 10^{-2}}$	$\mathbf{-5.1 \times 10^{-2}}$	-4.2×10^{-2}
ζ 950	-1.6×10^{-4}	$\mathbf{-3.1 \times 10^{-3}}$	-2.2×10^{-3}	$\mathbf{+1.3 \times 10^{-2}}$	-5.9×10^{-2}	$+4.0 \times 10^{-2}$
Θ_e(500 hPa) max	$+1.1 \times 10^{-5}$	$\mathbf{+5.5 \times 10^{-5}}$	$\mathbf{+9.5 \times 10^{-5}}$	$+1.2 \times 10^{-4}$	-2.6×10^{-3}	$+1.9 \times 10^{-3}$
Θ_e(500 hPa) mean	-3.6×10^{-6}	$+3.4 \times 10^{-6}$	$\mathbf{+4.3 \times 10^{-5}}$	$+7.8 \times 10^{-5}$	$+1.5 \times 10^{-5}$	$+1.3 \times 10^{-4}$
Θ(5 m) min	$+3.3 \times 10^{-5}$	$\mathbf{+3.4 \times 10^{-5}}$	-1.3×10^{-5}	$+5.6 \times 10^{-5}$	$\mathbf{+1.7 \times 10^{-3}}$	-2.4×10^{-4}
Θ(5 m) mean	-1.6×10^{-7}	-8.0×10^{-6}	-5.1×10^{-6}	$+7.2 \times 10^{-6}$	$\mathbf{+6.9 \times 10^{-4}}$	-8.8×10^{-4}

Table 11. Slope of fitting lines between diagnostic variables of the supercell and building heights (h_m, left block, units m^{-1}), or building density (λ_b, right block). Bolded values are statistically significant lower (or larger) then zero.

w700). In agreement with this result, the ensemble mean of the UH swath in the *h60* experiment (Fig. 8a) is higher than in the *h10* experiment (Fig. 8b).

In contrast, low-level storm diagnostic variables show a decreasing trend with increasing building height, and this trend is statistically significant lower than zero for some variables (e.g., $w950$ in the *city region*). This result is surprising and interesting, as it contrasts with the storm behavior aloft and also with the hypothesis that taller buildings should enhance vertical motions.

3.4 Building density

Variables describing the storm's mid-level characteristics show a general weakening trend in the *upstream* and *city regions* with increasing building density. However, this trend is statistically significant smaller than zero only for some variables (e.g., $w500$ and *ζ500*, Table 11). The mean UH does not exhibit a clear trend with increasing building density (Fig. S7). Low-level storm diagnostic variables do not show a consistent trend. In general, in the *downstream region*, no clear trend is observed either aloft or near the surface, and none of the studied variables exhibit statistically significant trends.

The ensemble mean of the UH swath shows slightly lower values *downstream* of the city in the $\lambda_b1.2$ experiment (Fig. 8d) compared to the $\lambda_b0.3$ experiment (Fig. 8c). Overall, we conclude that the storm does exhibit some sensitivity to building density; however, this parameter appears to be the least influential in determining storm dynamics among the previously studied parameters.

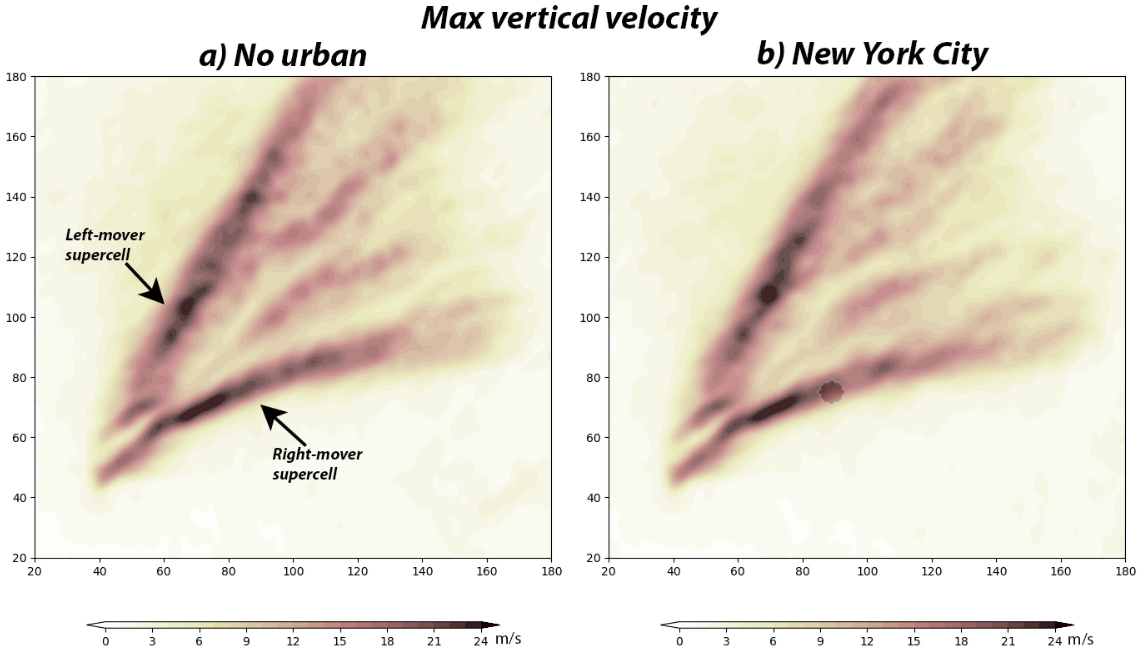

Figure 9. Ensemble mean of cumulated maximum vertical velocities in the a) *no_urban* and b) *NYC* experiment (Table 3). The city location is shown with a grey circular shading in b).

3.5 Additional experiments

Comparing Fig. 6c with Fig. 8e, it is evident that the weakening of the storm as it passes over the city is much less pronounced when the roofs are covered with vegetation (*green roof* experiment). Furthermore, using the rural energetic balance in the *no_thermo* experiment (Fig. 8f) results in a UH swath that is very similar to that of the *no_urban* experiment (Fig. 6a). Thus, the greater the amount of vegetation in a city, the less effect the city has on the approaching storm.

Lastly, no remarkable differences are observed whether the right-moving supercell passes over a rural area or over downtown NYC (experiment *NYC* in Table 3). The storm splitting attributed to NYC by Bornstein and Lin (2000) is not observed.

4 Results: Sensitivity of the pre-storm environment to the urban morphological parameters

To understand the urban effects on the simulated storm, we examine how urban morphological parameters influence near-surface variables, CAPE, SRH, and w950 at 04:00 pm (the time of convective initiation). This analysis compares ensemble-mean differences between simulations using the highest values of the morphological parameters ("max value" column in Table 3) and those using the lowest values ("zero value" column in Table 3).

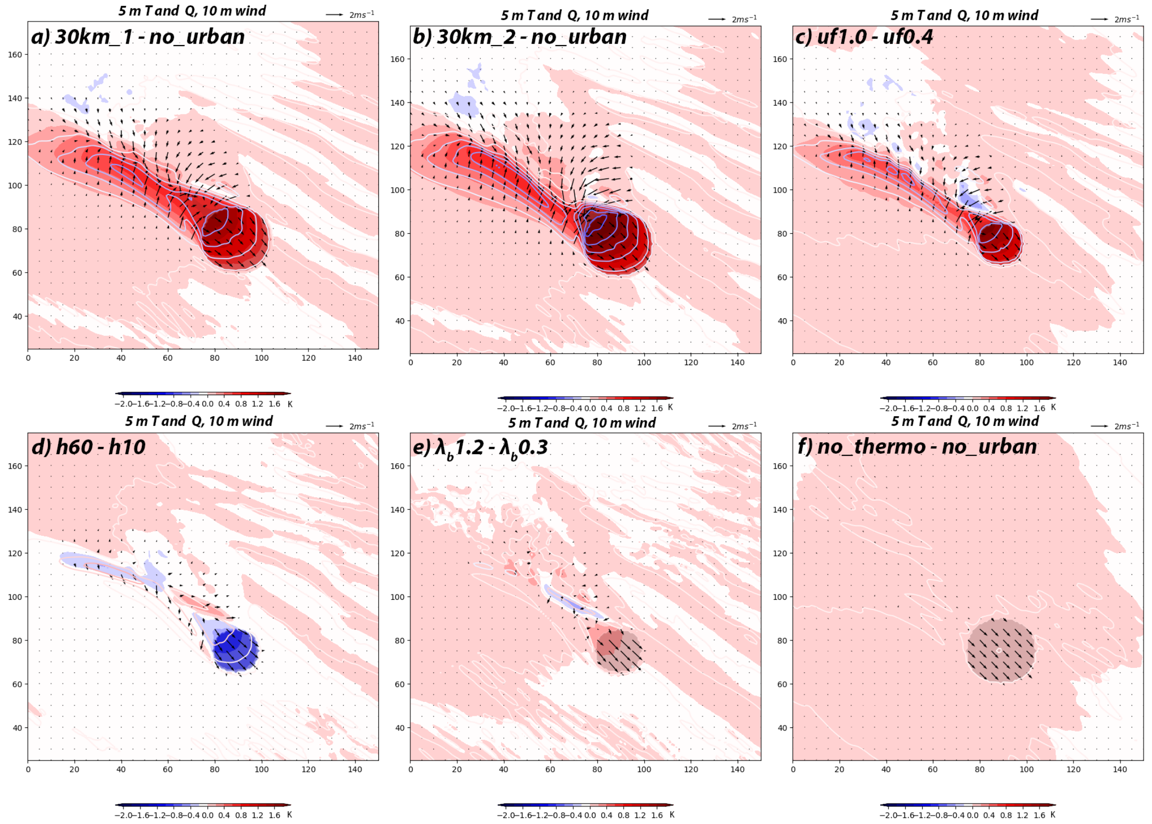

Figure 10. Ensemble mean of temperature (color shading) and specific humidity (contours every 0.5 g kg^{-1}, blue negative, red positive) in the first model level (about 5 m AGL), and 10-m wind difference (vectors) at 04:00 pm between a) *30km_1* and *no_urban* experiments; b) *30km_2* and *no_urban* experiments; c) *uf1.0* and *uf0.4* experiments; d) *h60* and *h10* experiments; e) $\lambda_b 1.2$ and $\lambda_b 0.3$ experiments; f) *green roofs* and *no_urban* experiment. The city is shown with grey shading.

4.1 Near-surface variables

The *30km_1* simulations produce a weak UHI of about 1.5 K over the city (Fig. 10a), in good agreement with typical daytime UHI magnitudes (Hidalgo et al., 2010). A pronounced UDI is also reproduced (peak of -2 gkg^{-1}), corresponding to a relative humidity difference of about 13% between the city and the surrounding rural areas, consistent with global observational studies (Meili et al., 2022). A wake of higher temperatures and lower humidity extends downwind (with respect to the southeasterly surface wind) up to 80 km from the city. Within this wake, a wind convergence is induced by the urban land use, while winds over the city are significantly reduced by increased drag. In the *30km_2* simulations, the UHI and UDI are slightly stronger, but the spatial pattern is similar (Fig. 10b). The urban-induced atmospheric modifications extend up to the top of the PBL, as shown in Figure S8, which displays the same variables as Figure 10 at the 850-hPa pressure level.

https://doi.org/10.5194/egusphere-2026-815
Preprint. Discussion started: 23 February 2026

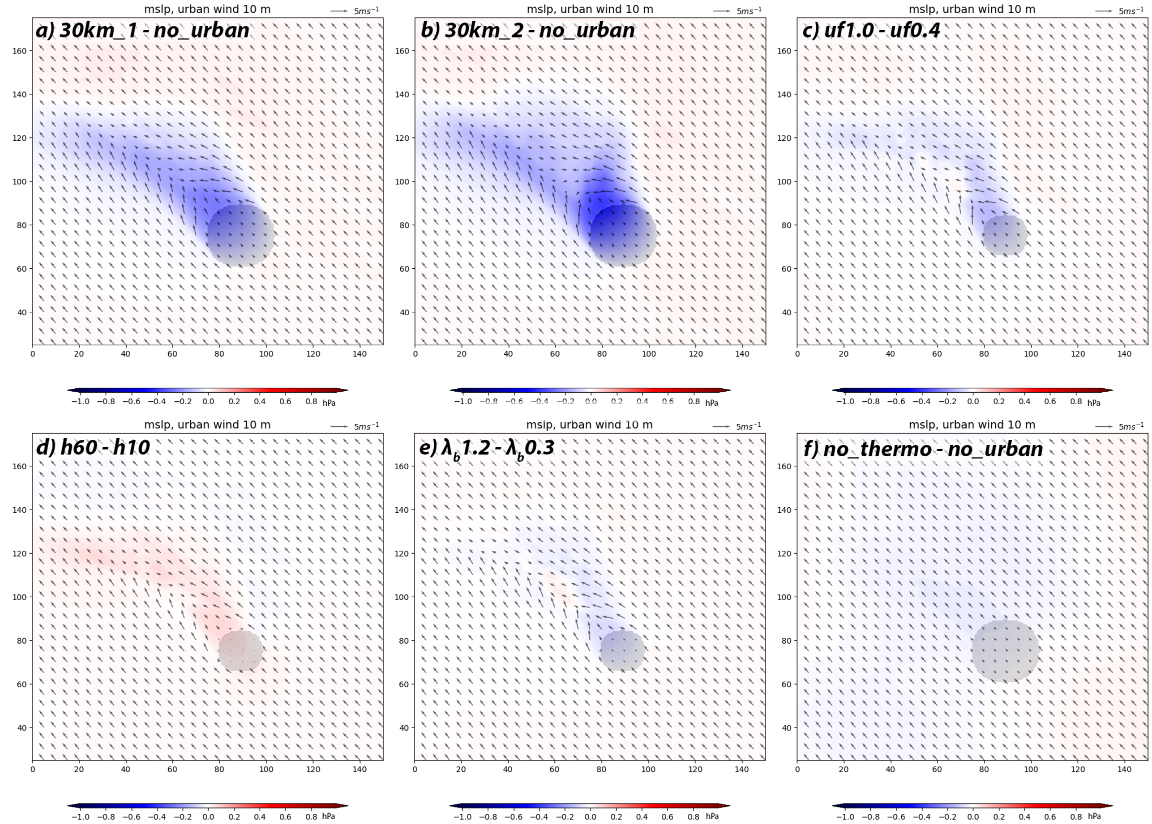

Figure 11. Ensemble mean of mean sea level pressure difference between a) *30km_1* and *no_urban* experiments; b) *30km_2* and *no_urban* experiments; c) *uf1.0* and *uf0.4* experiments; d) *h60* and *h10* experiments; e) λ_b*1.2* and λ_b*0.3* experiments; f) *green roofs* and *no_urban* experiments. The 10-m wind of the minuend simulation of the subtraction is shown with vectors. The city is shown with grey shading.

The impact of urban fraction on UHI and UDI is much smaller than that of city size, about 0.5 K and -1.0 g kg^{-1}, respectively (Fig. 10c). The downwind wind convergence is also weaker. A more compact city does not significantly alter the UHI or UDI but does reduce surface winds over the city (Fig. 10e).

An interesting result is that taller buildings reduce the UHI by about 1 K and increase moisture by 0.5 g kg^{-1} (Fig. 10d). Wind speeds are weaker in simulations with taller buildings, as well as the wind convergence downwind of the city. The reduction in temperature and increase in moisture in the urban canopy are likely due to reduced ventilation and consequent moisture stagnation (Wang et al., 2021). Our simulations begin with high moisture in the PBL, which decreases during the day due to mixing. In deeper urban canopies, drying is slower due to building shade, resulting in lower temperatures and higher moisture (Huang and Song, 2023).

Finally, in the *no_thermo* experiment, the UHI and UDI are eliminated, as expected, while maintaining the wind reduction over the city (Fig. 10f). This experiment can be interpreted as preserving the city's dynamic perturbation on the atmosphere (the weaker surface winds) while suppressing its thermodynamic effect (the UHI and UDI). Overall, city size is the factor with the most decisive influence on the UHI, consistent with previous studies (Zhou et al., 2017).

Regarding mean sea-level pressure, a weak minimum (about -0.5 hPa) is generated downwind of the city (with respect to the surface winds) by the urban land use (Fig. 11a). The downwind pressure minimum coincides with the wind convergence. With a higher urban fraction, the pressure minimum is stronger (about -1.0 hPa; Fig. 11b), as also suggested by the comparison between the *uf1.0* and *uf0.4* experiments (Fig. 11c). On the other hand, with taller buildings, the pressure minimum is slightly weaker (about 0.2 hPa; Fig. 11d), while a more compact city plays only a marginal role in intensifying it (Fig. 11e). Lastly, in the *no_thermo* experiment, the pressure minimum is absent.

A relationship between the UHI and the mean sea-level pressure is evident: in simulations with a stronger UHI (e.g., *30km_2* experiment), the pressure minimum is also stronger, whereas when the UHI is weaker (*h60* experiment) or absent (*no_thermo* experiment), the pressure minimum is weaker or absent. Thus, it appears that the pressure minimum is thermodynamically induced by the UHI (i.e., it is a consequence of the buoyancy and not of the dynamical modification of the flow by the buildings). To further support this hypothesis, an additional analysis is carried out. The dynamic p'_d and buoyancy p'_b pressure perturbations are computed for the ensemble mean of the *30km_2* simulations. The reference p_0 value is taken from the ensemble mean of the *no_urban* experiment. Figure 12 shows the results at the 10th vertical level (about 300 m AGL). Buoyancy pressure perturbations p'_b clearly dominate the generation of the downstream pressure minimum, consistent with the previously noted sensitivity between the pressure minimum and the intensity of the UHI. The contribution of the dynamic pressure perturbations p'_d is negligible. This outcome is also valid for the *h60* experiment (Fig. 12d,e,f): tall buildings have a marginal effect on the generation of the downwind pressure minimum with respect to the thermodynamic modification of the PBL induced by urban land use.

4.2 CAPE

CAPE is markedly reduced by urban land use along a wake downstream of the city (Fig. 13a,b). The reduction in CAPE reaches up to 1000 J kg^{-1} and coincides with the wake of higher temperature and lower moisture observed in Fig. 10. Urban fraction contributes to a decrease in CAPE of about 200 J kg^{-1} (Fig. 13c), while taller buildings increase CAPE by up to 400 J kg^{-1} (Fig. 13d). Building density has no significant effect on CAPE (Fig. 13e), consistent with the results previously discussed for other near-surface variables. In the *no_thermo* experiment, CAPE is unaffected by the presence of the buildings (Fig. 13f).

The same sensitivity of CAPE to urban morphological parameters observed for moisture suggests that the decrease in moisture more than offsets the temperature increase, which alone would enhance CAPE. While the UHI drives the generation of the downwind pressure minimum, the UDI drives the formation of the wake with reduced CAPE.

4.3 Vertical Velocities at 950 hPa

To assess the city's capacity to trigger convection, the differences in ensemble means of vertical velocity at 950 hPa are analyzed. Upstream and over the city, remarkable vertical velocities are not induced by urban land use (Fig. 14a,b). In contrast, downstream of the city, a line of intensified vertical velocity extends up to 60 km from the city. In the *30km_2* experiment,

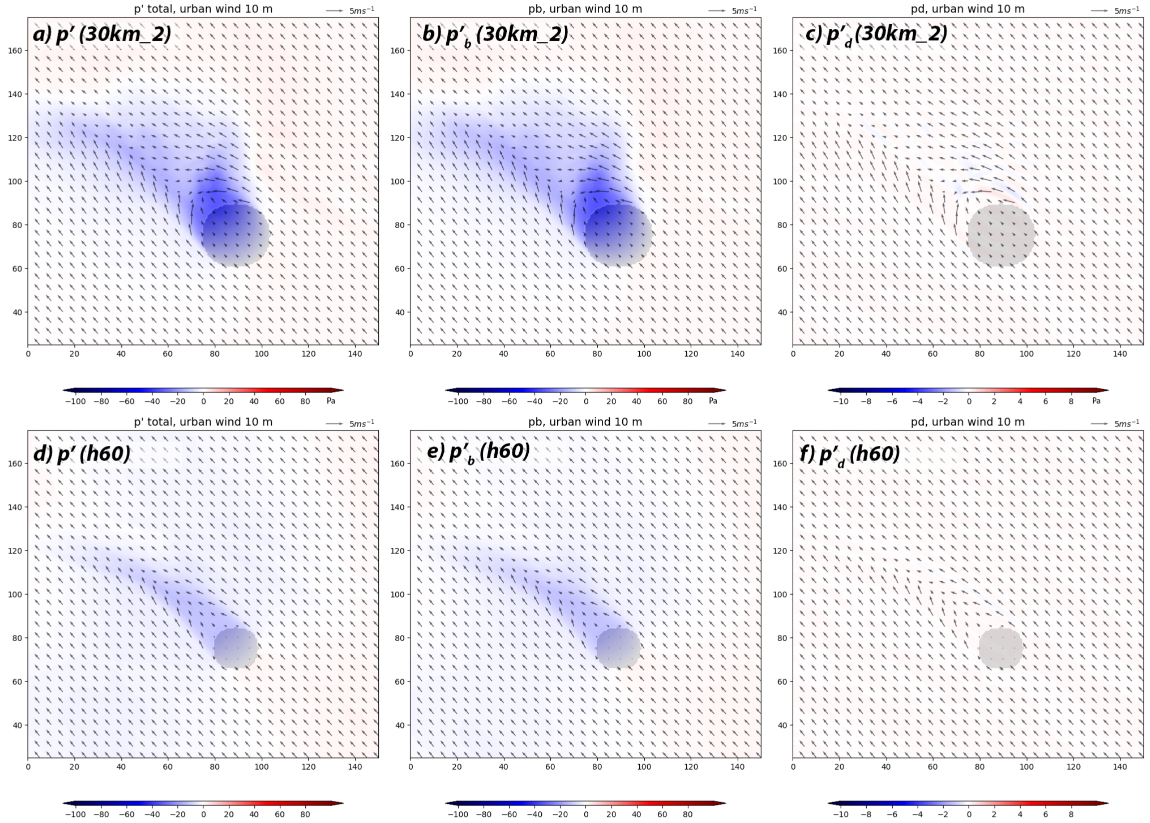

Figure 12. Ensemble mean of a) total pressure perturbations p' at 300m AGL in the *30km_2* experiment; b) as in a) but for buoyancy pressure perturbations p'_b; c) as in b) but for dynamic pressure perturbations p'_d; d), e) and f) as in a), b) and c), respectively, but for the *h60* experiment.

the intensified vertical velocity reaches locally up to 1 m s^{-1}. This line coincides with the surface wind convergence. A higher urban fraction produces stronger vertical velocities (Fig. 14c), while taller buildings reduce their intensity (Fig. 14d). A more compact city slightly intensifies vertical velocities downstream (Fig. 14e), whereas vertical velocities are not produced in the *no_thermo* experiment (Fig. 14f).

The intensification of vertical velocities is related to the intensity of the UHI. A stronger UHI leads to a deeper pressure minimum, more vigorous surface wind convergence, and stronger vertical velocities. For example, in the simulation with taller buildings, vertical velocities are weaker (Fig. 14d) because both the pressure minimum (Fig. 11d) and the UHI (Fig. 10d) are weaker. In the *no_thermo* experiment, vertical velocities are absent (Fig. 14f) because neither a pressure minimum (Fig. 11f) nor a UHI (Fig. 10f) develops. The effect of building height is therefore negligible: even buildings as tall as 60 m do not lead to an intensification of vertical velocities. This result explains why low-level vertical velocities in the simulated supercell do not increase with increasing building height, as discussed in Section 33.3.

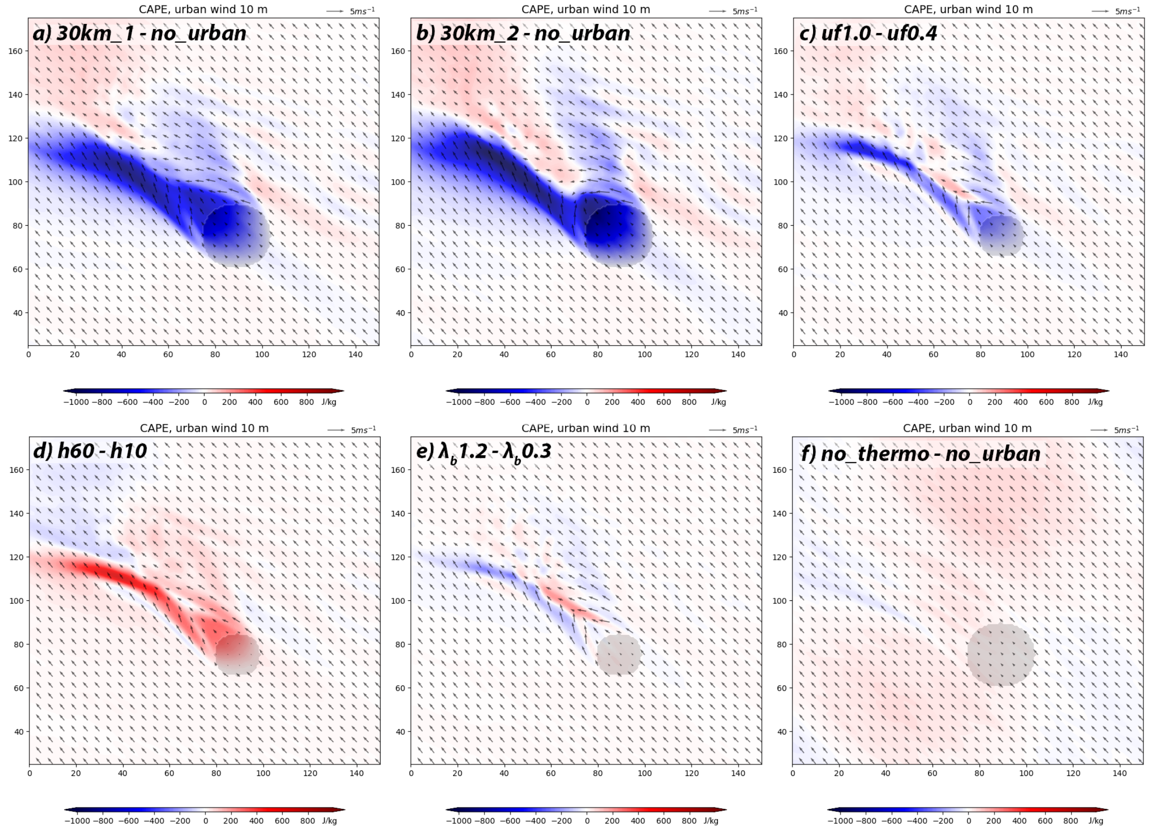

Figure 13. As in Fig. 11, but for CAPE.

4.4 Wind Shear: SRH 0-3 km

In the *30km_1* and *30km_2* experiments, SRH 0–3 km is reduced by up to 100 J kg^{-1} (about 50 % less than in the *no_urban* simulations) south of the convergence line discussed in Section 4.3, and increased north of it with a similar magnitude (Fig. 15a). The increase (reduction) of SRH north (south) of the convergence line is due to the greater (smaller) veering of the wind caused by a stronger (weaker) surface easterly wind component (Fig. 10a) and a stronger pressure minimum. Thus, the modifications of SRH are ultimately induced by the pressure minimum generated by the UHI. The urban fraction amplifies this SRH pattern (Fig. 15c). In contrast, taller buildings cause the opposite pattern, i.e., higher SRH values south of the convergence line, due to the weaker pressure minimum. In the *building density* and *no_thermo* experiments, the SRH is almost unperturbed, except for slightly higher values over the city (Fig. 15e,f). The increase of SRH over the city results from reduced surface winds (Fig. 10e,f), consistent with the findings of Reames and Stensrud (2018).

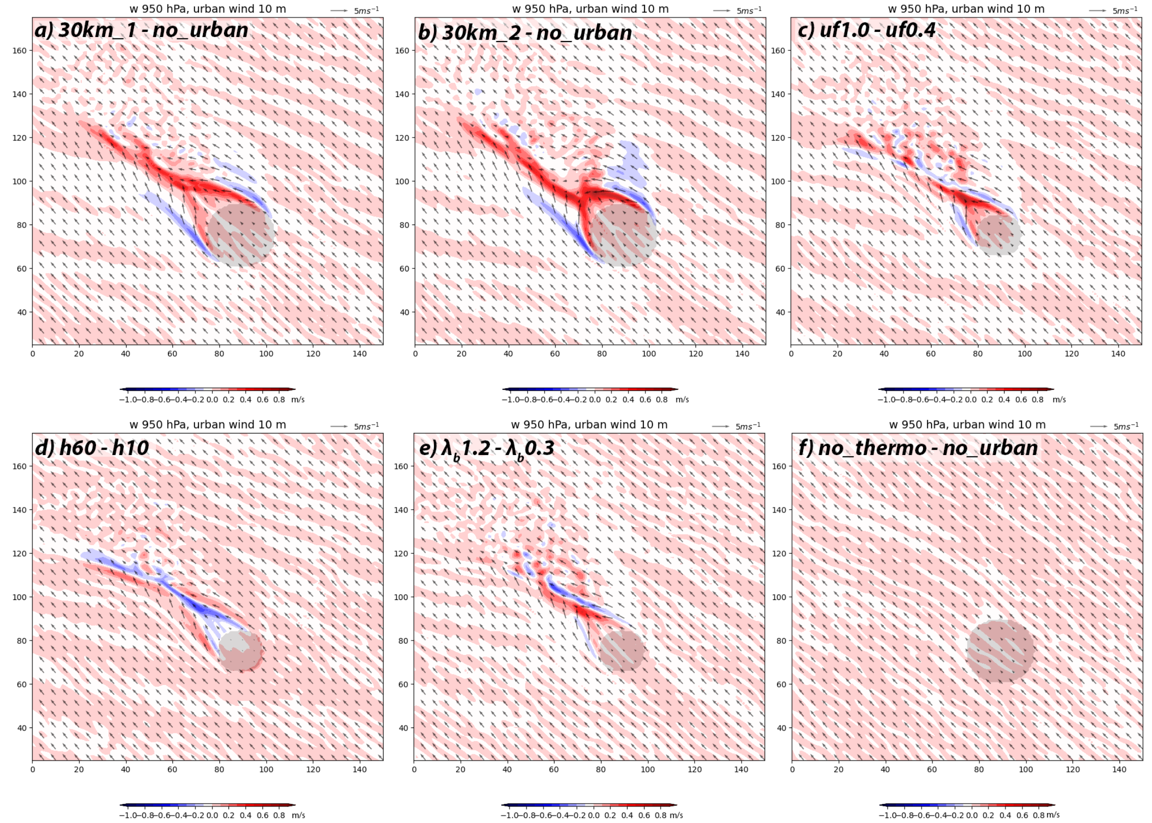

Figure 14. As in Fig. 11, but for vertical velocities at 950 hPa.

5 Discussion

In the current study, the ensembles of idealized numerical experiments consistently show a weakening of a supercell moving into a city due to the urban land use, especially downstream of the city. This weakening is significant primarily in medium- to large-sized cities with a high urban fraction (Fig. 5). For smaller cities, the effect is less evident and not statistically significant, with some ensemble members showing that the supercell is even intensified. The weakening of the supercell is caused by the UDI, which drives a substantial reduction in CAPE, up to 1000 J kg^{-1} (Fig. 13), in the wake downstream of the city (relative to the surface winds, Fig. 16a). Previous studies have also found that urban land use can reduce CAPE (e.g., Reames and Stensrud 2018; Yang et al. 2014); however, to the authors' knowledge, this is the first time that an urban-induced reduction of CAPE has been directly linked to an urban-induced weakening of storms. Our conclusions differ markedly from those of Naylor and Mulholland (2023); Naylor et al. (2024), who did not consider the UDI in their idealized setup. This factor proves crucial in shaping supercell dynamics in our simulations. These outcomes also differ from those of Lin et al. (2021), probably because the city they considered, Kansas City, has a low mean urban fraction and the confluence of two large rivers lies at the heart of the city, both of which likely result in a comparatively suppressed UDI.

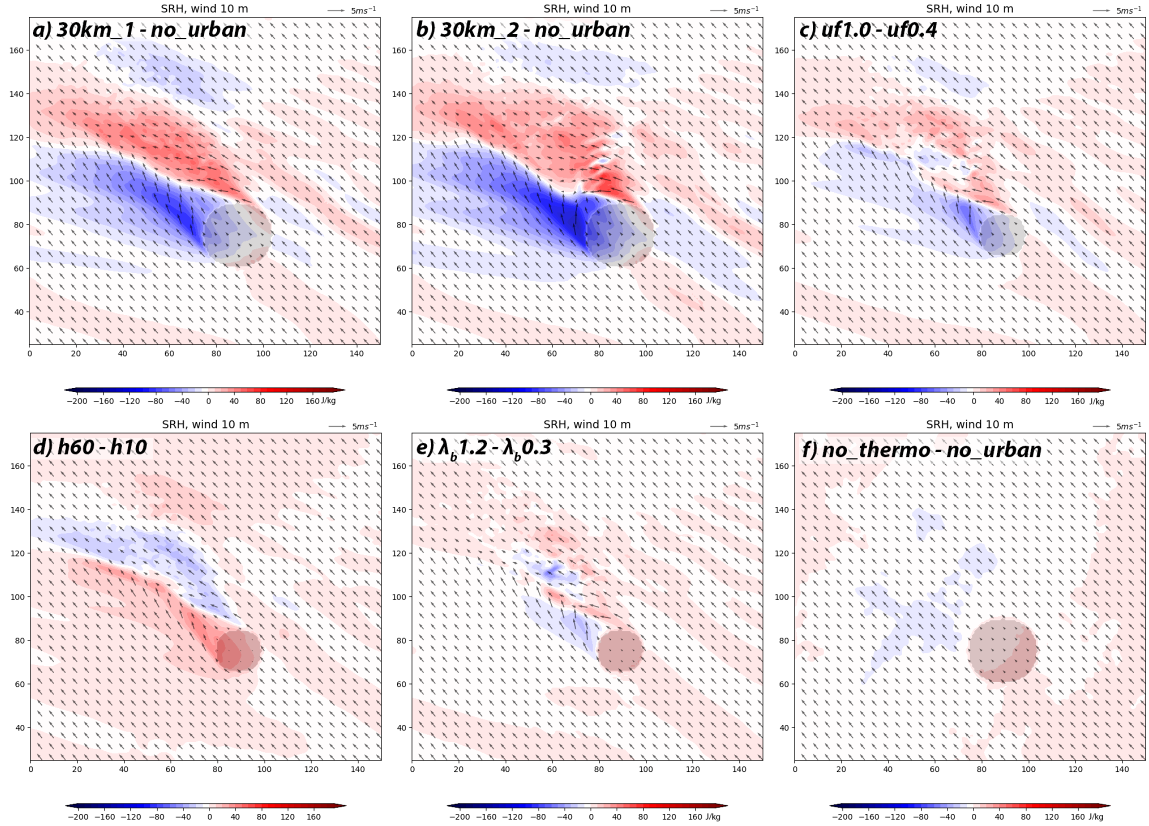

Figure 15. As in Fig. 11 but for SRH 0-3 km.

With a sufficiently large city and a high urban fraction, a new urban-induced supercell develops in 8 out of 11 ensemble members downstream of the city, while the initial incoming supercell is dissipated by the UDI (e.g., Fig. 7). This new urban-induced supercell is triggered by a convergence line downstream of the city, generated by a pressure minimum of about 1 hPa (Fig. 16a). The UHI thermodynamically induces a pressure minimum, as it was already suggested by Rozoff et al. (2003), which in turn produces the convergence line (Fig. 11). The connection between the pressure minimum and the UHI is supported by a quantitative analysis of pressure perturbations (Fig. 12) and by an *ad-hoc* experiment called *no_thermo*. Although in our experiments the generation of the urban-induced supercell occurs only with a 30-km-wide city and an urban fraction of 1.0, it could also occur with smaller cities and lower urban fractions. The key requirement may simply be a sufficiently strong UHI combined with an environment conducive to supercells. In our numerical simulations, the threshold for the development of an urban-induced supercell corresponds to a UHI of 1.5 K, which is not particularly high.

There is some observational evidence supporting these numerical results. The radar-based climatological study of Kingfield et al. (2018) found that, for four Great Plains cities in the United States, reflectivity values of approaching storms were higher upwind than downwind. The opposite pattern was observed, however, when selecting an urban-favorable subset of nonsuper-

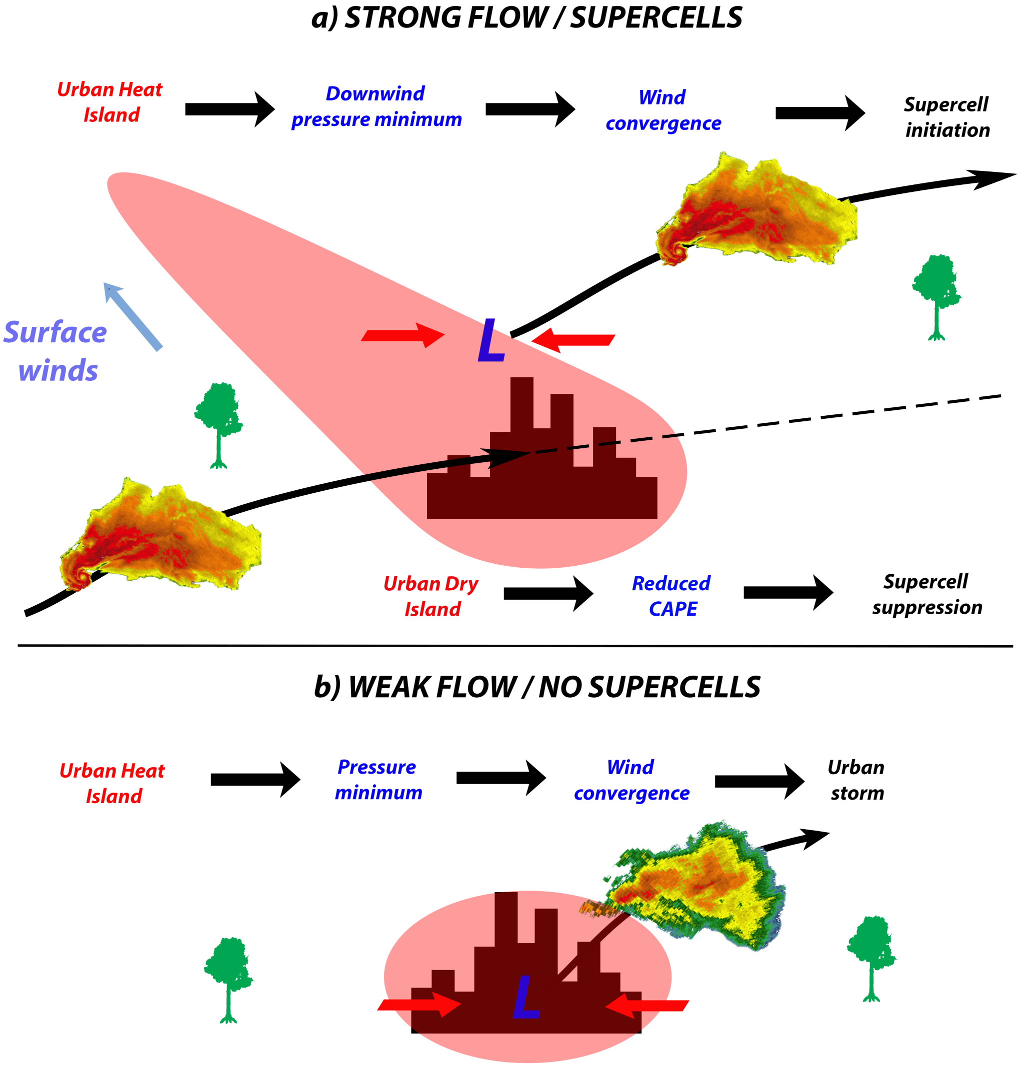

Figure 16. a) Conceptual model for the interaction of supercell storms with a city: the UHI and UDI (red shading), city (black histogram), supercell (yellowish-reddish shading with hook-echo shape), pressure minumum (letter L) and wind convergence (red arrows) are shown. b) as in a), but for a weak flow situation without supercells.

cells occurring during summer under weak synoptic forcing. Similarly, the radar-based study of Lorenz et al. (2019) found that storms striking Berlin were more frequently weakened than intensified. Thus, in strongly forced environments, it is not uncommon for approaching storms to be dissipated or weakened by cities, as is observed in our numerical simulations. This scenario has received relatively little attention in the literature, as most studies have focused on the potential of cities to generate urban storms and enhance precipitation (e.g., Shen and Yang 2023; Shepherd et al. 2002). The latter outcome is likely common in weakly forced synoptic environments and can also occur at times under strongly forced conditions. However, the weakening of severe storms by urban land use is an equally important outcome that should be highlighted. Similarly, the capability of cities to generate their own supercell, as highlighted in this work, has not been emphasized in past studies, with few exceptions (Reames and Stensrud, 2018; Lin et al., 2021).

An additional relevant difference from previous works is that the effect of building height on storms is negligible in our experiments, even with 60 m tall buildings. In these cases, the pressure minimum is still induced by the UHI (Fig. 12), and the vertical velocities generated by 60-m tall buildings are much weaker than those associated with the UHI-induced pressure minimum (Fig. 14d). Furthermore, building height is not correlated with higher values of low-level vertical velocities in the simulated supercell (Table 11). The building-barrier effect (Bornstein and LeRoy, 1990) was explicitly tested with an *ad-hoc* experiment using an NYC-like city and was also found to be negligible. These results are consistent with the recently published work of Torelló-Sentelles et al. (2025), who found that the enhanced vertical velocities observed over some real cities in their simulations were primarily driven by thermodynamic processes rather than by dynamical roughness effects. Thus, there is growing agreement that the dynamical influence of buildings on convective storms may be marginal in a synoptically forced environment. Nevertheless, the building-barrier effect could still play a role in other strongly forced situations not explored in these idealized simulations, such as QLCS events with intense outflows (e.g., De Martin et al. 2025).

The marginal effect of buildings on convective storms is likely valid for most atmospheric environments (Torelló-Sentelles et al., 2025). If building height has little impact on storms under relatively strong surface flows, its influence should be even less relevant in weakly forced environments. For this reason, we argue that our conceptual model can be extended to such environments. Under weak flow conditions, the UHI-induced pressure minimum is not advected downstream but remains centered over the urban area, as also suggested by some recent case study analysis (Swain et al., 2025; Kawabata et al., 2025; Forster et al., 2024; Seino et al., 2018). Consequently, storms can be triggered over the urban area in such situations.

6 Conclusions

The simulations carried out in this work permit to provide a tentative answer to the questions originally posed in the Introduction.

Question 1: *Can a city modify a supercell?*

A statistically significant weakening of the approaching supercell is observed. In contrast, in some ensemble members, a new supercell is triggered downstream when a sufficiently large city is included in the domain, highlighting the dual effect of cities on supercell storms.

Question 2*: What are the physical processes that cause those modifications?*

Most of the observed modifications are attributed to thermodynamic changed in the PBL induced by urban surfaces. The UDI weakens an approaching storm by reducing CAPE. At the same time, the UHI generates a pressure minimum, capable of inducing downstream wind convergence that can trigger a new urban-induced supercell when the UHI is sufficiently intense. The effect of building heights on supercell dynamics is considered negligible.

These results significantly advance our understanding of the interactions between urban land use and severe storms. A further interesting outcome of this work is the simulated supercell's sensitivity to surface conditions. Relatively small differences in temperature (1 K) and moisture (1 g kg^{-1}) are sufficient to alter supercell behavior markedly. A direct implication of this result is that operational weather-forecasting models must be driven by up-to-date land-use data. For instance, changes in vegetation caused by drought, if not assimilated into the models, can lead to significantly inaccurate forecasts (see also Zhang et al. 2025).

Although the analysis presented here is robust, several limitations remain that should be addressed in future work. In the model employed, small-scale urban processes—which may, in some situations, strongly influence urban storms (e.g., under shallow surface-based inflow layers)—are not directly represented. Large Eddy Simulations (LES) should be conducted (as done by Rozoff et al. 2023 for hurricane winds) to assess the importance of these processes for convective storms and to test whether the results of this study hold under that approach. Furthermore, some studies showed that urban aerosols can significantly influence storm development (Liu and Niyogi, 2019; Fan et al., 2020; Lin et al., 2021), suggesting that the effect of urban aerosols on idealized supercells may be worthy of investigation. Another aspect not considered here includes the effects of urban land use on nocturnal events: while the UHI is stronger during the night, nocturnal storms are usually elevated, suggesting that urban-storm interactions may differ from those during the daytime. Lastly, idealized simulations of a QLCS, rather than a supercell, interacting with a city should also carried out to evaluate whether building effects on the gust front may dominate over the UHI and UDI in such cases.

Acknowledgements. FDM acknowledges the I-CHANGE project, funded by the European Union's Horizon 2020 research and innovation programme under grant agreement No. 101037193. SDS acknowledges the TRIGGER project, funded by the European Union's Horizon Europe research and innovation programme under grant agreement No. 101057739. We acknowledge high-performance computing support from the Derecho system (doi:10.5065/qx9a-pg09) provided by the NSF National Center for Atmospheric Research (NCAR), sponsored by the National Science Foundation. Rich Rotunno, George Bryan, Alberto Martilli, Jason Keeler, Eric Hendricks, Wesley Terwey, and Patrick Hawbecker are gratefully acknowledged for fruitful discussions on the setup of the simulations. We acknowledge the use of ChatGPT for code debugging and minor text revisions.

https://doi.org/10.5194/egusphere-2026-815
Preprint. Discussion started: 23 February 2026

Author contributions. The study was conceptualized by FDM, AZ, and SDS. The software was provided by AZ, while the formal analysis was conducted by FDM, CR, and SA. Computational resources were provided by CR and SA, while SDS supervised the work and secured funding. FDM wrote the original draft, which was edited by CR, AZ, SA, and SDS.

Competing interests. The authors declare that they have no conflict of interest.

References

Andrews, M. S., Gensini, V. A., Haberlie, A. M., Ashley, W. S., Michaelis, A. C., and Taszarek, M.: Climatology of the Elevated Mixed Layer over the Contiguous United States and Northern Mexico Using ERA5: 1979–2021, Journal of Climate, 37, 1833 – 1851, https://doi.org/10.1175/JCLI-D-23-0517.1, 2024.

Berner, J., Shutts, G., Leutbecher, M., and Palmer, T.: A spectral stochastic kinetic energy backscatter scheme and its impact on flow-dependent predictability in the ECMWF ensemble prediction system, Journal of the Atmospheric Sciences, 66, 603–626, https://doi.org/https://doi.org/10.1175/2008JAS2677.1, 2009.

Bornstein, R. and LeRoy, M.: Urban barrier effects on convective and frontal thunderstorms, in: Extended Abstracts, Fourth Conf. on Mesoscale Processes, pp. 120–121, 1990.

Bornstein, R. and Lin, Q.: Urban heat islands and summertime convective thunderstorms in Atlanta: Three case studies, Atmospheric Environment, 34, 507–516, https://doi.org/https://doi.org/10.1016/S1352-2310(99)00374-X, 2000.

Bougeault, P. and Lacarrere, P.: Parameterization of orography-induced turbulence in a mesobeta–scale model, Monthly weather review, 117, 1872–1890, https://doi.org/https://doi.org/10.1175/1520-0493(1989)117<1872:POOITI>2.0.CO;2, 1989.

Boyer, C. H., Keeler, J. M., and Rakoczy, B. C.: An Idealized Parameter Study of Destabilization and Convection Initiation in Coastal Regions. Part I: Calm or Offshore Synoptic-Scale Flow, Journal of the Atmospheric Sciences, 82, 519 – 539, https://doi.org/10.1175/JAS-D-23-0180.1, 2025.

Britter, R. E. and Hanna, S. R.: Flow and dispersion in urban areas, Annual review of fluid mechanics, 35, 469–496, https://doi.org/https://doi.org/10.1146/annurev.fluid.35.101101.161147, 2003.

Changnon, S. A. and Ackerman, B.: Summary of METROMEX, Volume 1: Weather anomalies and impacts, Bulletin (Illinois State Water Survey) no. 62, 1977.

Ching, J., Mills, G., Bechtel, B., See, L., Feddema, J., Wang, X., Ren, C., Brousse, O., Martilli, A., Neophytou, M., et al.: WUDAPT: An urban weather, climate, and environmental modeling infrastructure for the anthropocene, Bulletin of the American Meteorological Society, 99, 1907–1924, 2018.

Coffer, B. E., Parker, M. D., Peters, J. M., and Wade, A. R.: Supercell Low-Level Mesocyclones: Origins of Inflow and Vorticity, Monthly Weather Review, 151, 2205 – 2232, https://doi.org/10.1175/MWR-D-22-0269.1, 2023.

Dahl, J. M. L. and Fischer, J.: The Origin of Western European Warm-Season Prefrontal Convergence Lines, Weather and Forecasting, 31, 1417 – 1431, https://doi.org/10.1175/WAF-D-15-0161.1, 2016.

De Martin, F., Zonato, A., and Di Sabatino, S.: Effects of the urban land use on a severe convective windstorm, Quarterly Journal of the Royal Meteorological Society, n/a, e5058, https://doi.org/https://doi.org/10.1002/qj.5058, 2025.

Dou, J., Wang, Y., Bornstein, R., and Miao, S.: Observed Spatial Characteristics of Beijing Urban Climate Impacts on Summer Thunderstorms, Journal of Applied Meteorology and Climatology, 54, 94 – 105, https://doi.org/10.1175/JAMC-D-13-0355.1, 2015.

Dou, J., Bornstein, R., Sun, J., and Miao, S.: Impacts of urban heat island intensities on a bifurcating thunderstorm over Beijing, Urban Climate, 55, 101 955, https://doi.org/https://doi.org/10.1016/j.uclim.2024.101955, 2024.

Dudhia, J.: Numerical Study of Convection Observed during the Winter Monsoon Experiment Using a Mesoscale Two-Dimensional Model, Journal of Atmospheric Sciences, 46, 3077 – 3107, https://doi.org/10.1175/1520-0469(1989)046<3077:NSOCOD>2.0.CO;2, 1989.

Emanuel, K.: On the Physics of High CAPE, Journal of the Atmospheric Sciences, 80, 2669 – 2683, https://doi.org/10.1175/JAS-D-23-0060.1, 2023.

Fan, J., Zhang, Y., Li, Z., Hu, J., and Rosenfeld, D.: Urbanization-induced land and aerosol impacts on sea-breeze circulation and convective precipitation, Atmospheric Chemistry and Physics, 20, 14 163–14 182, https://doi.org/https://doi.org/10.5194/acp-20-14163-2020, 2020.

Fan, J., Wang, J., and Lin, Y.: Urbanization may enhance tornado potential: A single case report, Frontiers in Earth Science, 11, 1148 506, https://doi.org/https://doi.org/10.3389/feart.2023.1148506, 2023.

Forster, A., Augros, C., and Masson, V.: Urban influence on convective precipitation in the Paris region: Hectometric ensemble simulations in a case study, Quarterly Journal of the Royal Meteorological Society, 150, 3028–3051, https://doi.org/https://doi.org/10.1002/qj.4749, 2024.

Hao, L., Sun, G., Huang, X., Tang, R., Jin, K., Lai, Y., Chen, D., Zhang, Y., Zhou, D., Yang, Z.-L., et al.: Urbanization alters atmospheric dryness through land evapotranspiration, npj Climate and Atmospheric Science, 6, 149, https://doi.org/https://doi.org/10.1038/s41612-023-00479-z, 2023.

Heimann, D. and Kurz, M.: The Munich hailstorm of July 12, 1984: a discussion of the synoptic situation, Beiträge zur Physik der Atmosphäre, 58, 528–544, 1985.

Hidalgo, J., Masson, V., and Gimeno, L.: Scaling the daytime urban heat island and urban-breeze circulation, Journal of Applied Meteorology and Climatology, 49, 889–901, https://doi.org/https://doi.org/10.1175/2009JAMC2195.1, 2010.

Homeyer, C. R., Bunkers, M. J., Allen, J. T., and Murphy, A. M.: United States Supercell Storms and Their Severity: A 14-yr Radar-Based Climatology, Journal of Applied Meteorology and Climatology, 2025.

Hong, S.-Y., Noh, Y., and Dudhia, J.: A New Vertical Diffusion Package with an Explicit Treatment of Entrainment Processes, Monthly Weather Review, 134, 2318 – 2341, https://doi.org/10.1175/MWR3199.1, 2006.

Huang, X. and Song, J.: Urban moisture and dry islands: spatiotemporal variation patterns and mechanisms of urban air humidity changes across the globe, Environmental Research Letters, 18, 103 003, https://doi.org/10.1088/1748-9326/acf7d7, 2023.

Janjić, Z. I.: The step-mountain eta coordinate model: Further developments of the convection, viscous sublayer, and turbulence closure schemes, Monthly weather review, 122, 927–945, https://doi.org/https://doi.org/10.1175/1520-0493(1994)122<0927:TSMECM>2.0.CO;2, 1994.

Jiménez, P. A., Dudhia, J., González-Rouco, J. F., Navarro, J., Montávez, J. P., and García-Bustamante, E.: A Revised Scheme for the WRF Surface Layer Formulation, Monthly Weather Review, 140, 898 – 918, https://doi.org/10.1175/MWR-D-11-00056.1, 2012.

Kamath, H. G., Singh, M., Malviya, N., Martilli, A., He, L., Aliaga, D., He, C., Chen, F., Magruder, L. A., Yang, Z.-L., et al.: GLObal Building heights for Urban Studies (UT-GLOBUS) for city-and street-scale urban simulations: development and first applications, Scientific Data, 11, 886, https://doi.org/https://doi.org/10.1038/s41597-024-03719-w, 2024.

Kawabata, T., Saya, A., Nishi, A., Seino, N., Hayashi, S., Ito, J., Ikuta, Y., and Seko, H.: Simulating a Thunderstorm using a High-Resolution Ensemble and an Urban Canopy Model: A Test Case for RDP Paris, SOLA, https://doi.org/https://doi.org/10.2151/sola.2025-048, 2025.

Kingfield, D. M., Calhoun, K. M., de Beurs, K. M., and Henebry, G. M.: Effects of city size on thunderstorm evolution revealed through a multiradar climatology of the central United States, Journal of Applied Meteorology and Climatology, 57, 295–317, https://doi.org/https://doi.org/10.1175/JAMC-D-16-0341.1, 2018.

Lin, Y., Min, Q., Zhuang, G., Wang, Z., Gong, W., and Li, R.: Spatial features of rain frequency change and pollution and associated aerosols, Atmospheric Chemistry and Physics, 11, 7715–7726, https://doi.org/https://doi.org/10.5194/acp-11-7715-2011, 2011.

Lin, Y., Fan, J., Jeong, J.-H., Zhang, Y., Homeyer, C. R., and Wang, J.: Urbanization-induced land and aerosol impacts on storm propagation and hail characteristics, Journal of the Atmospheric Sciences, 78, 925–947, https://doi.org/https://doi.org/10.1175/JAS-D-20-0106.1, 2021.

Liu, J. and Niyogi, D.: Meta-analysis of urbanization impact on rainfall modification, Scientific reports, 9, 7301, https://doi.org/https://doi.org/10.1038/s41598-019-42494-2, 2019.

Lorenz, J. M., Kronenberg, R., Bernhofer, C., and Niyogi, D.: Urban rainfall modification: Observational climatology over Berlin, Germany, Journal of Geophysical Research: Atmospheres, 124, 731–746, https://doi.org/https://doi.org/10.1029/2018JD028858, 2019.

Manzato, A., Serafin, S., Miglietta, M. M., Kirshbaum, D., and Schulz, W.: A pan-Alpine climatology of lightning and convective initiation, Monthly Weather Review, 150, 2213–2230, https://doi.org/https://doi.org/10.1175/MWR-D-21-0149.1, 2022.

Markowski, P. M. and Dotzek, N.: A numerical study of the effects of orography on supercells, Atmospheric research, 100, 457–478, https://doi.org/https://doi.org/10.1016/j.atmosres.2010.12.027, 2011.

Martilli, A., Clappier, A., and Rotach, M. W.: An urban surface exchange parameterisation for mesoscale models, Boundary-layer meteorology, 104, 261–304, https://doi.org/https://doi.org/10.1023/A:1016099921195, 2002.

Meili, N., Paschalis, A., Manoli, G., and Fatichi, S.: Diurnal and seasonal patterns of global urban dry islands, Environmental Research Letters, 17, 054 044, https://doi.org/10.1088/1748-9326/ac68f8, 2022.

Mlawer, E. J., Taubman, S. J., Brown, P. D., Iacono, M. J., and Clough, S. A.: Radiative transfer for inhomogeneous atmospheres: RRTM, a validated correlated-k model for the longwave, Journal of Geophysical Research: Atmospheres, 102, 16 663–16 682, https://doi.org/https://doi.org/10.1029/97JD00237, 1997.

Morrison, H., Thompson, G., and Tatarskii, V.: Impact of Cloud Microphysics on the Development of Trailing Stratiform Precipitation in a Simulated Squall Line: Comparison of One- and Two-Moment Schemes, Monthly Weather Review, 137, 991 – 1007, https://doi.org/10.1175/2008MWR2556.1, 2009.

Naylor, J.: Idealized simulations of city-storm interactions in a two-dimensional framework, Atmosphere, 11, 707, https://doi.org/https://doi.org/10.3390/atmos11070707, 2020.

Naylor, J. and Mulholland, J.: The impact of vertical wind shear on the outcome of interactions between squall lines and cities, Journal of Geophysical Research: Atmospheres, 128, e2022JD037 237, https://doi.org/https://doi.org/10.1029/2022JD037237, 2023.

Naylor, J., Berry, M. E., and Gosney, E. G.: Idealized Simulations of a Supercell Interacting with an Urban Area, Meteorology, 3, 97–113, https://doi.org/https://doi.org/10.3390/meteorology3010005, 2024.

Niu, G.-Y., Yang, Z.-L., Mitchell, K. E., Chen, F., Ek, M. B., Barlage, M., Kumar, A., Manning, K., Niyogi, D., Rosero, E., Tewari, M., and Xia, Y.: The community Noah land surface model with multiparameterization options (Noah-MP): 1. Model description and evaluation with local-scale measurements, Journal of Geophysical Research: Atmospheres, 116, https://doi.org/https://doi.org/10.1029/2010JD015139, 2011.

Nowotarski, C. J., Markowski, P. M., Richardson, Y. P., and Bryan, G. H.: Properties of a Simulated Convective Boundary Layer in an Idealized Supercell Thunderstorm Environment, Monthly Weather Review, 142, 3955 – 3976, https://doi.org/10.1175/MWR-D-13-00349.1, 2014.

Oke, T. R.: The energetic basis of the urban heat island, Quarterly Journal of the Royal Meteorological Society, 108, 1–24, https://doi.org/https://doi.org/10.1002/qj.49710845502, 1982.

Pappaccogli, G., Giovannini, L., Zardi, D., and Martilli, A.: Sensitivity analysis of urban microclimatic conditions and building energy consumption on urban parameters by means of idealized numerical simulations, Urban Climate, 34, 100 677, https://doi.org/https://doi.org/10.1016/j.uclim.2020.100677, 2020.

Platonov, V., Varentsov, M., Yarinich, Y. I., Shikhov, A., and Chernokulsky, A.: A large mid-latitude city intensifies severe convective events: Evidence from long-term high-resolution simulations, Urban Climate, 54, 101 837, https://doi.org/https://doi.org/10.1016/j.uclim.2024.101837, 2024.

Reames, L. J. and Stensrud, D. J.: Influence of a Great Plains urban environment on a simulated supercell, Monthly Weather Review, 146, 1437–1462, https://doi.org/https://doi.org/10.1175/MWR-D-17-0284.1, 2018.

Romine, G. S., Schwartz, C. S., Berner, J., Fossell, K. R., Snyder, C., Anderson, J. L., and Weisman, M. L.: Representing forecast error in a convection-permitting ensemble system, Monthly Weather Review, 142, 4519–4541, https://doi.org/https://doi.org/10.1175/MWR-D-14-00100.1, 2014.

Rotunno, R. and Klemp, J. B.: The influence of the shear-induced pressure gradient on thunderstorm motion, Monthly Weather Review, 110, 136–151, https://doi.org/https://doi.org/10.1175/1520-0493(1982)110<0136:TIOTSI>2.0.CO;2, 1982.

Rozoff, C. M., Cotton, W. R., and Adegoke, J. O.: Simulation of St. Louis, Missouri, land use impacts on thunderstorms, Journal of Applied Meteorology and Climatology, 42, 716–738, https://doi.org/https://doi.org/10.1175/1520-0450(2003)042<0716:SOSLML>2.0.CO;2, 2003.

Rozoff, C. M., Nolan, D. S., Bryan, G. H., Hendricks, E. A., and Knievel, J. C.: Large-eddy simulations of the tropical cyclone boundary layer at landfall in an idealized urban environment, Journal of Applied Meteorology and Climatology, 62, 1457–1478, https://doi.org/https://doi.org/10.1175/JAMC-D-23-0024.1, 2023.

Salamanca, F., Krpo, A., Martilli, A., and Clappier, A.: A new building energy model coupled with an urban canopy parameterization for urban climate simulations—part I. formulation, verification, and sensitivity analysis of the model, Theoretical and applied climatology, 99, 331–344, https://doi.org/https://doi.org/10.1007/s00704-009-0142-9, 2010.

Seino, N., Oda, R., Sugawara, H., and Aoyagi, T.: Observations and simulations of the mesoscale environment in TOMACS urban heavy rain events, Journal of the Meteorological Society of Japan. Ser. II, 2018.

Shen, Y. and Yang, L.: Divergent urban signatures in rainfall anomalies explained by pre-storm environment contrast, Geophysical Research Letters, 50, e2022GL101 658, https://doi.org/https://doi.org/10.1029/2022GL101658, 2023.

Shepherd, J. M.: Impacts of urbanization on precipitation and storms: Physical insights and vulnerabilities, Climate Vulnerability, Volume 5, 109-125, 5, 109–125, https://doi.org/https://doi.org/10.1016/B978-0-12-384703-4.00503-7, 2013.

Shepherd, J. M., Pierce, H., and Negri, A. J.: Rainfall modification by major urban areas: Observations from spaceborne rain radar on the TRMM satellite, Journal of applied meteorology, 41, 689–701, https://doi.org/https://doi.org/10.1175/1520-0450(2002)041<0689:RMBMUA>2.0.CO;2, 2002.

Skamarock, W. C., Klemp, J. B., Dudhia, J., Gill, D. O., Liu, Z., Berner, J., Wang, W., Powers, J. G., Duda, M. G., Barker, D. M., et al.: A description of the advanced research WRF version 4, NCAR tech. note ncar/tn-556+ str, 145, 2019.

Swain, M., Peña, J. C., Bornstein, R. D., and González-Cruz, J. E.: Coastal and anthropogenic heat impacts on PBL processes during extreme summer thunderstorm precipitation in New York City, Urban Climate, 62, 102 534, https://doi.org/https://doi.org/10.1016/j.uclim.2025.102534, 2025.

Terwey, W. D. and Rozoff, C. M.: Objective convective updraft identification and tracking: Part 1. Structure and thermodynamics of convection in the rainband regions of two hurricane simulations, Journal of Geophysical Research: Atmospheres, 119, 6470–6496, https://doi.org/https://doi.org/10.1002/2013JD020904, 2014.

Thielen, J. and Gadian, A.: Influence of topography and urban heat island effects on the outbreak of convective storms under unstable meteorological conditions: a numerical study, Meteorological Applications, 4, 139–149, https://doi.org/https://doi.org/10.1017/S1350482797000303, 1997.

Torelló-Sentelles, H., Koukoula, M., Villarini, G., Marra, F., and Peleg, N.: When storms slow down: urban effects on rainfall accumulation and flood hazard, npj Natural Hazards, 2, 106, 2025.

Tuckman, P. and Emanuel, K.: Origins of Extreme CAPE around the World, Journal of Geophysical Research: Atmospheres, 129, e2024JD041 833, https://doi.org/https://doi.org/10.1029/2024JD041833, 2024.

Virtanen, P., Gommers, R., Oliphant, T. E., Haberland, M., Reddy, T., Cournapeau, D., Burovski, E., Peterson, P., Weckesser, W., Bright, J., van der Walt, S. J., Brett, M., Wilson, J., Millman, K. J., Mayorov, N., Nelson, A. R. J., Jones, E., Kern, R., Larson, E., Carey, C. J., Polat, İ., Feng, Y., Moore, E. W., VanderPlas, J., Laxalde, D., Perktold, J., Cimrman, R., Henriksen, I., Quintero, E. A., Harris, C. R., Archibald, A. M., Ribeiro, A. H., Pedregosa, F., van Mulbregt, P., and SciPy 1.0 Contributors: SciPy 1.0: Fundamental Algorithms for Scientific Computing in Python, Nature Methods, 17, 261–272, https://doi.org/10.1038/s41592-019-0686-2, 2020.

Wang, Z., Song, J., Chan, P. W., and Li, Y.: The urban moisture island phenomenon and its mechanisms in a high-rise high-density city, International Journal of Climatology, 41, E150–E170, https://doi.org/https://doi.org/10.1002/joc.6672, 2021.

Weisman, M. L. and Klemp, J. B.: The dependence of numerically simulated convective storms on vertical wind shear and buoyancy, Monthly Weather Review, 110, 504–520, https://doi.org/https://doi.org/10.1175/1520-0493(1982)110<0504:TDONSC>2.0.CO;2, 1982.

Wurman, J., Alexander, C., Robinson, P., and Richardson, Y.: Low-level winds in tornadoes and potential catastrophic tornado impacts in urban areas, Bulletin of the American Meteorological Society, 88, 31–46, https://doi.org/https://doi.org/10.1175/BAMS-88-1-31, 2007.

Yang, L., Tian, F., Smith, J. A., and Hu, H.: Urban signatures in the spatial clustering of summer heavy rainfall events over the Beijing metropolitan region, Journal of Geophysical Research: Atmospheres, 119, 1203–1217, https://doi.org/https://doi.org/10.1002/2013JD020762, 2014.

Yang, L., Li, Q., Yuan, H., Niu, Z., and Wang, L.: Impacts of urban canopy on two convective storms with contrasting synoptic conditions over Nanjing, China, Journal of Geophysical Research: Atmospheres, 126, e2020JD034 509, https://doi.org/https://doi.org/10.1029/2020JD034509, 2021a.

Yang, L., Ni, G., Tian, F., and Niyogi, D.: Urbanization Exacerbated Rainfall Over European Suburbs Under a Warming Climate, Geophysical Research Letters, 48, e2021GL095 987, https://doi.org/https://doi.org/10.1029/2021GL095987, e2021GL095987 2021GL095987, 2021b.

Yang, L., Yang, Y., Shen, Y., Yang, J., Zheng, G., Smith, J., and Niyogi, D.: Urban development pattern's influence on extreme rainfall occurrences, Nature communications, 15, 3997, https://doi.org/https://doi.org/10.1038/s41467-024-48533-5, 2024.

Yang, Z.-L., Niu, G.-Y., Mitchell, K. E., Chen, F., Ek, M. B., Barlage, M., Longuevergne, L., Manning, K., Niyogi, D., Tewari, M., and Xia, Y.: The community Noah land surface model with multiparameterization options (Noah-MP): 2. Evaluation over global river basins, Journal of Geophysical Research: Atmospheres, 116, https://doi.org/https://doi.org/10.1029/2010JD015140, 2011.

Zhang, Y., Miao, S., Dai, Y., and Bornstein, R.: Numerical simulation of urban land surface effects on summer convective rainfall under different UHI intensity in Beijing, Journal of Geophysical Research: Atmospheres, 122, 7851–7868, https://doi.org/https://doi.org/10.1002/2017JD026614, 2017.

Zhang, Z., He, C., Chen, F., Miguez-Macho, G., Liu, C., and Rasmussen, R.: US Corn Belt enhances regional precipitation recycling, Proceedings of the National Academy of Sciences, 122, e2402656 121, https://doi.org/https://doi.org/10.1073/pnas.240265612, 2025.

Zhou, B., Rybski, D., and Kropp, J. P.: The role of city size and urban form in the surface urban heat island, Scientific reports, 7, 4791, https://doi.org/https://doi.org/10.1038/s41598-017-04242-2, 2017.

Zonato, A., Martilli, A., Gutierrez, E., Chen, F., He, C., Barlage, M., Zardi, D., and Giovannini, L.: Exploring the effects of rooftop mitigation strategies on urban temperatures and energy consumption, Journal of Geophysical Research: Atmospheres, 126, e2021JD035 002, https://doi.org/https://doi.org/10.1029/2021JD035002, 2021.